Investigation of aero-hydro-elastic-mooring behavior of a H-type floating vertical axis wind turbine using coupled CFD-FEM method.

Qingsong Liu [a, c], Musa Bashir [b], Gregorio Iglesias [d, e], Weipao Miao [a, *], Minnan Yue [a], Zifei Xu [c], Yang Yang [f], Chun Li[a]

[a] *School of Energy and Power Engineering, University of Shanghai for Science and Technology, Shanghai, 200093. P.R. China*
[b] *School of Engineering, University of Liverpool, The Quadrangle, Brownlow Hill, L69 3GH, United Kingdom*
[c] *Liverpool Logistics, Offshore and Marine (LOOM) Research Institute, Liverpool John Moores University, Liverpool, Byrom Street, L3 3AF, United Kingdom.*
[d] *School of Engineering, Computing and Mathematics (SECaM), University of Plymouth, Plymouth, PL48 AA, United Kingdom.*
[e] *School of Engineering and Architecture, University College Cork, Ireland, T12 K8AF, UK*
[f] *Faculty of Maritime and Transportation, Ningbo University, Ningbo 315211, China.*

Abstract

Floating vertical axis wind turbines (VAWTs) are being explored as a promising new option for harnessing offshore wind energy due to their unique advantages, including low installation and maintenance costs, high operational efficiency in wind farm clusters, and scalability of rotor sizes. However, the lack of software capable of simulating the aeroelastic of VAWTs poses a significant barrier to their further development and deployment. The aim of this paper is to develop a fully coupled aero-hydro-elastic-mooring-material model for floating VAWTs. The aerodynamic performance, hydrodynamic response and structural nonlinearities of the floating VAWT are analyzed in detail using Computational Fluid Dynamics (CFD) and the Finite Element Method (FEM). The results indicate that: (i) The dynamic response of the floating VAWT platform results in more pronounced fluctuations in the power coefficient, characterized by frequent spike-like extreme values, compared to fixed VAWT. Nevertheless, wake dissipation in floating VAWT is quicker, facilitating faster flow recovery and a more marked acceleration effect in the flow field. (ii) The surge and pitch motions of the platform affect the velocity of the blades relative to the fluid, resulting in additive and subtractive effects with the incoming flow. This interaction gives the blade torque of the floating VAWT an alternating performance advantage in the upwind region, compared to fixed VAWT; (iii) Stress analysis reveals that the highest levels of stress occur at the juncture between the support arm and the blade, with significant stress also present at the bottom of the central pontoon. In contrast, the blade tips exhibit the lowest stress levels. (iv) The blades of the floating VAWT undergo radial deformation due to wind loads and centrifugal forces, while the support arms experience vertical vibrations, driven by their own weight combined with that of the blades. (v) The mooring lines, particularly influenced by platform traction and frequent interactions with the seabed, show dynamic shifts in maximum contact pressures, especially between moorings C2 and C3. Mooring C2, located on the windward side, consistently faces more intense seabed interactions.

Keywords: Floating VAWT; Aeroelastic; Computational fluid dynamics; Finite element analysis; Fluid-Structure Interaction.

1. Introduction

1.1. The renaissance of floating VAWT

Wind energy is widely recognized for its potential to provide a clean and sustainable source of renewable energy, playing a pivotal role in mitigating the emissions of harmful greenhouse gases [1]. In recent years, research in offshore wind energy has seen a notable increase [2]. However, conventional bottom-fixed turbine foundations are economically viable only within a restricted range of sea depths

(< 60 m). In deeper waters, the deployment of floating platforms becomes imperative [3-4].

Horizontal axis wind turbines (HAWTs), which are currently the predominant choice in floating wind development, have reached a mature state of technological development. However, concerns about their stability in turbulent offshore environments persist. Maintenance and repair efforts within maritime settings can also pose considerable challenges. Furthermore, the blades of HAWTs experience cyclically reversing gravitational loads, necessitating continuous technological improvements in blade materials and manufacturing processes to achieve cost reductions for large turbines [5].

In exploring alternatives to enhance offshore wind competitiveness, VAWTs are currently under investigation. Unlike HAWTs, VAWTs experiences oscillating aerodynamic loads during operation, which offer a more advantageous scaling behavior than gravitational loads [6].

In an offshore context, VAWTs might require smaller and potentially less costly floating platforms compared to those needed for HAWTs [7,8]. The reason is that HAWTs have the drivetrain and generator placed high above the water level, creating large overturning moments. To counter these moments, the floating platform typically needs additional mass in the substructure (Fig. 1). This issue is less critical for VAWTs because the drivetrain and generator are positioned closer to the water level. Additionally, VAWTs do not require a yaw mechanism since they are insensitive to the wind direction.

These factors are anticipated to enhance the scalability of VAWTs, potentially leading to reduced costs of offshore installations in future developments [9], as indicated by preliminary studies of Ennis et al [10], which suggest a cost reduction of up to 25% in certain scenarios.

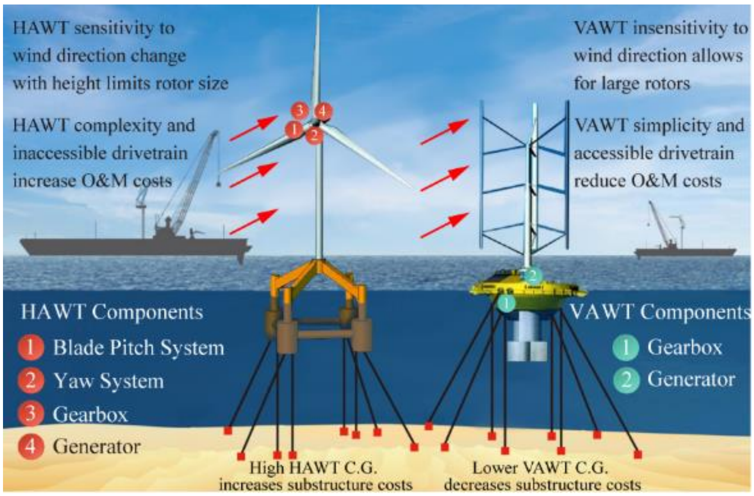

Fig. 1. Comparison of offshore HAWT and VAWT

1.2. Research challenges

Floating VAWTs have attracted considerable attention from researchers due to several advantages when installed at offshore sites. However, it is evident from the literature that the development of floating VAWTs is still in its infancy. Although various rotor designs with floating substructures have been studied [11,12], and various VAWT concepts [13-16] have been proposed and investigated, the optimal floating VAWT design remains elusive, unlike their horizontal axis counterparts.

Designing a floating VAWT involves the challenge of accurately predicting critical loads due to variable turbulent wind and stochastic wave conditions [17]. Precisely calculating these critical loads is immensely challenging due to the complex multi-physical phenomena occurring under real operational conditions. Consequently, there is a significant need to enhance the development and application of an advanced numerical analysis method. This method should be capable of comprehensively considering the complex multi-physical phenomena resulting from the aero-hydro-multibody dynamics of a floating VAWT model in actual operational scenarios.

Currently, the hydrodynamic behavior of floating offshore wind turbines (FOWTs) is predominantly analyzed using conventional hydrodynamic software like AQWA and WAMIT, as well as specific numerical codes tailored for FOWTs, including 3Dfloat, DeepC, HAWC2, SIMO, Bladed, and F2A [18-21]. Despite their utility, these methodologies fall short in offering comprehensive insights into the flow dynamics around turbine blades, the distribution of aerodynamic loads, or the characteristics of the vortex wake behind the turbine. This gap hinders effective management of the Fluid-Structure Interaction (FSI) in FOWTs, the handling of turbine blade stall, and the dynamic responses of the floating platforms.

Furthermore, the absence of readily available software for comprehensive aero-elastic simulations, especially for VAWTs incorporating composite materials, poses a significant barrier. This limitation obstructs the assessment of structural performance and suitability for offshore environments. As load calculations are a prerequisite for designing all other turbine components, this represents a major obstacle to the further development of VAWTs and leaves their potential advantages in Levelized Cost of Energy (LCOE) unclear.

1.3. Overview of research for evaluation of floating VAWT

The research on VAWTs predominantly utilizes experimental studies and numerical simulations, specifically focusing on micro-scale VAWTs. Experimental studies, primarily conducted through wind tunnel experiments [22-24], include measuring the aerodynamic performance, thrust, and wake characteristics of rotors, thus providing essential benchmark validation for numerical computations.

CFD has been extensively employed to investigate the unsteady aerodynamics of VAWTs due to its capability to capture critical flow information like wake patterns and vortex structures. Key research areas include active and passive flow control techniques to mitigate dynamic stall and flow separation in VAWTs [25, 26], wake studies [27, 28], and investigations into parameters influencing simulations, such as turbulence models [29], grid size [30], convergence criteria [31], domain scale and time steps [32]. Additionally, studies on three-dimensional flow effects [33] and the virtual incidence [34, 35] have also provided deeper insights into the complex aerodynamics of VAWTs.

However, most of the aforementioned studies have focused on small land based VAWTs, with little research conducted on large-scale VAWTs involving structural and material properties. The main reason for this discrepancy is that structural nonlinearities are not prominent in small VAWTs, where blades are usually assumed to be rigid or mono-metallic. In contrast, large-scale VAWTs must be designed with structural loads in mind, rendering simplifying rigidity assumptions impractical.

In the realm of research concerning floating VAWTs, two primary approaches emerged: uncoupled and partially coupled analyses. The aim of conducting an uncoupled analysis is to simplify the simulation of a floating VAWT and optimize computational efficiency. Through the application of overlapping grid or chimera grid techniques, the platform motion is examined under specific degrees of freedom (DOF), thus facilitating the study of its impact on the aerodynamic behavior of the VAWT.

Fig. 2 illustrates the motion pattern of the platform for a floating VAWT using an uncoupled method. Initially, the rotor is positioned at its equilibrium point, with the blades' azimuth angle set at 0 degrees. The computational process does not account for the floating platform and mooring lines. Instead, a set of predefined sinusoidal functions is applied to the overlapping mesh domain to simulate the surge and pitch motions of platform. The sequence of motions follows this pattern: 1→2→3.

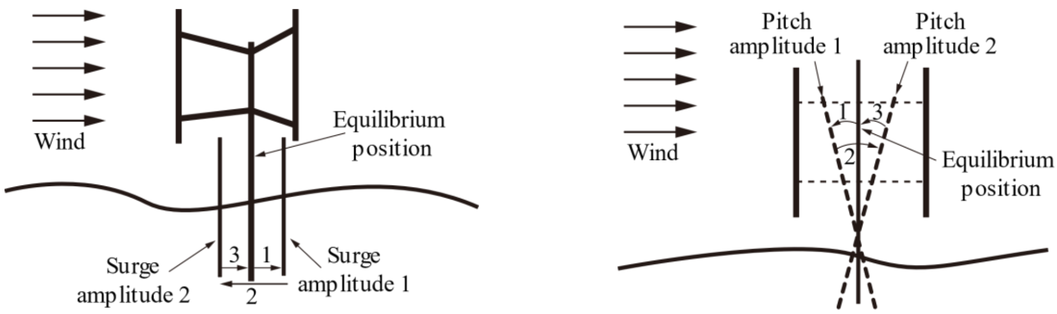

(a) Surge motion (b) Pitch motion

Fig. 2 Schematic diagram of movement for floating VAWT.

Lei et al. [36] used the overlapping grid modeling technique to simulate the aerodynamic behavior of a small H-type VAWT subjected to a prescribed surge motion. Their findings revealed that employing a smaller surge amplitude with a longer surge period can improve the stability of floating VAWT operation, resulting in a more consistent power output. Su et al [37] employed a comparable methodology to examine the influence of pitch motion on the aerodynamic performance of a φ-type VAWT. Their study revealed that platform pitch can be considered as a combination of surge and heave motions, which can enhance the VAWT power coefficient, albeit at the cost of increased load fluctuations. In a recent study conducted by Kuang et al. [38], two tandem VAWTs were positioned within a computational domain to investigate the rotor wake characteristics. In this study, the upstream VAWT executed a prescribed pitching motion using the overlapping grid technique. The results demonstrated that, in comparison to a bottom-fixed tandem VAWTs configuration, the pitching motion of the upstream VAWT altered the wake deficit away from the central region. This modification reduced the wake interference experienced by the downstream VAWT, thereby enhancing its dynamic performance. The studies mentioned above simplify simulations by omitting significant interactions among the rotor, platform, and mooring lines. While these simplified models serve as valuable initial approximations, they may not encompass the complete spectrum of intricate interactions and dynamic effects essential for the design, optimization, and safety assurance of offshore VAWTs. As such, researchers and engineers can use these approaches as starting points, but it becomes imperative to transition towards coupled simulations to obtain more precise and comprehensive insights.

The coupled analysis represents a significant advancement in understanding the complex interaction between the motion of the platform and the aerodynamic performance of VAWT. These analyses offer a more holistic and realistic view of how VAWTs behave in offshore environments. In recent years, researchers have been actively working on the development of coupled models that go even further by considering the interaction between wind and waves. This added complexity allows for a more accurate assessment of the aerodynamic and hydrodynamic characteristics of floating VAWTs.

Table 1 summarizes the current state of coupling tools used for simulating floating VAWTs. These tools encompass a wide range of computational methods, software packages, and modeling techniques designed to capture the intricate dynamics of VAWTs in offshore conditions.

Table 1 - Partially coupled analyses relative to floating VAWT.

Tools	Aerodynamics	Hydrodynamics	Structural dynamics	Blade Materials	Mooring dynamics
OWENS [39]	CACTUS	Airy + PF + ME	FEM	Beam	UDF

FloVAWT [40]	DMS +DS	Airy + PF + ME	–	–	QS
CALHYPSO [41]	DMS +DS	Airy+ PF +ME	–	Beam, single material	QS
SIMO-RIFLEX-DMS [42]	DMS + DS	Airy + PF +ME	FEM	Beam, single material	FEM
SIMO-RIFLEX-AC [43]	AC + DS	Airy +PF + ME	FEM	Beam, single material	FEM
DFBI [44]	SST k-ω Turbulence model	VOF wave model	–	Rigid	QS

DMS, double multi-streamtube method; DS, dynamic stall; AC, actuator cylinder flow method; Airy, airy wave theory; PE, potential flow; ME, Morison' equation; VOF, Volume of Fluid; QS, quasi static. UDF, user-defined force

1.4. Research gap and motivation

The coupled tools highlighted in Table 1 offer valuable insights into the simulation of VAWTs. However, they come with specific limitations and areas for improvement:

- DMS and AC methods are advantageous for their simplicity and ability to estimate VAWT performance. However, they often simplify complex blade interactions [45], which can lead to inaccuracies, especially when dealing with strong turbulences interactions between blades. Improving these methods to better capture blade interactions is crucial for accurate performance predictions, especially in densely packed arrays of VAWTs.
- Hydrodynamic simulations mainly using potential flow theory have limitations in accurately capturing flow behavior near the surface of floating platforms. Viscous effects near the platform surface can be significant, and potential flow theory may not fully account for these effects [46]. Advanced modeling approaches that incorporate viscous effects or more sophisticated CFD methods could lead to more accurate hydrodynamic simulations.
- Quasi-static methods are commonly used for modeling moorings. While these methods simplify the modeling process, they often ignore nonlinearities that can arise from factors like line stretching or interactions with the seabed. Neglecting these nonlinearities may lead to conservative estimates of mooring tensions [47]. Developing more sophisticated and dynamic mooring models that account for these nonlinearities is essential for accurately predicting the behavior of mooring systems.
- Previous studies have paid less attention to the aeroelastic behavior of VAWT blades, particularly when considering composite materials. As floating VAWTs continue to grow in size, understanding the aeroelastic behavior of these blades under high coupling conditions is crucial [48]. This includes accounting for the dynamic interactions between the rotor, platform motion, and composite materials to ensure the structural integrity and optimal performance of the blades.

In summary, while the coupled tools presented in Table 1 provide valuable insights into floating VAWTs, there are opportunities for refinement and advancement in each of these areas to enhance accuracy, especially as offshore wind turbines continue to evolve in complexity and size.

1.5. Present work

The primary objective of this paper is to develop a fully coupled model that can comprehensively analyze the aerodynamics, hydrodynamics, structural nonlinearities, and mooring dynamics of floating VAWTs. To achieve this, a high-fidelity CFD approach is employed to simulate the viscous effects of fluid, wave propagation, and the complex interactions between the VAWT structures (such as blades, support arms, and towers) and the fluid. The FEM method is used to analyze the structural stress and deformation of the floating VAWT, the aeroelastic behavior of composite material blades, and the contact effects between the moorings and the seabed.

The innovations of this paper are summarized as follows:

- This paper offers a comprehensive account of geometric modeling, material property configurations, fluid-structure coupling settings. To the best of the authors' knowledge, this work represents a pioneering effort to analyze the aeroelastic behavior and structural nonlinearities of a floating VAWT.
- Previous studies on floating VAWTs typically assume that the platform is rigid and ignores the effects of ballast water. Furthermore, mooring modelling has mainly involved quasi-static simulations, overlooking the interaction of the moorings with the seabed. Such simplifications have led to underestimation of mooring tension and the production of inaccurate results. For the first time, the present study analyzes the structural response of floating platforms as well as the contact effects between the moorings and the seabed.
- The fully coupled model presented in the paper can be applied to a broader range of scenarios beyond floating VAWTs. With appropriate adjustments to the geometric modeling, it can be utilized for floating HAWTs, ships with moorings, and other scenarios involving fluid-structure interactions. This versatility makes it a valuable tool for understanding and analyzing complex systems in the marine environment.

The outline of this paper is as follows: Section 2 presents the numerical theory and methodology employed. Section 3 details the geometrical model used in this study, specifically elaborating the composite layup scheme for the floating VAWT blades, along with the material properties of the platform and mooring system. Section 4 primarily addresses the reliability and accuracy in the validation of the proposed fully coupled method. Section 5 presents the results and discussion, focusing on the aerodynamics, hydrodynamics, and structural nonlinearities of the floating VAWT. Section 6 summarizes the main conclusions and suggests possible future works.

2. Methodology

2.1. Coupling strategy

In this study, a fully coupled aero-elastic-hydro-mooring-material model for floating VAWTs is developed using coupled CFD-FEM method:

- The Finite Volume Method (FVM), combined with Reynolds-Averaged Navier-Stokes (RANS) based SST k-ω turbulence model, is employed in STAR-CCM+ to simulate the effects of fluid viscosity, wave diffraction, radiation, slamming, and climbing accurately. A segregated flow solver is used to sequentially solve the integral conservation equations for mass and momentum. This solver incorporates a pressure-velocity coupling algorithm that ensures mass conservation in the velocity field by solving a pressure-correction equation. Additionally, the second-order upwind scheme is employed to compute the convective fluxes, enhancing the simulation accuracy.
- The FEM is employed in ABAQUS to discretize the components of the floating VAWT, including the blades, support arms, tower, platform, mooring, and seabed. AQUA, a specialized module of ABAQUS, is used to compute the inertial forces, drag, and buoyancy affecting the mooring system in a marine environment. This analysis incorporates the composite material properties of the blades, the ballast water in the platform, and the contact effects between the mooring and the seabed. Such integration facilitates a comprehensive evaluation of structural nonlinearities.
- The SIMULIA Co-Simulation Engine from Dassault Systèmes enables communication between ABAQUS and STAR-CCM+ during the co-simulation analyses of floating VAWT. In this setup,

STAR-CCM+ exports traction data, including pressure and wall shear stress, to ABAQUS and imports nodal displacements. The two software packages exchange fields through a shared interface. The ABAQUS Explicit Coupling scheme is used to manage the frequency of data exchange per time step. This integrated approach enhances the accurate in calculating the aero-elastic response of the VAWT.

- The Volume of Fluid (VOF) multiphase model in STAR-CCM+ is employed to track the movement and distribution of the air-water interface, which is disturbed by the floating platform. This implementation allows for the real-time update of the spatial distribution of the air and water two-phase flow.

2.2. The VOF waves model

The VOF multiphase model is an interface-capturing technique employed within STAR-CCM+ software for predicting the behavior of immiscible fluid phases and their respective interfaces in CFD simulations. This method proves particularly effective for simulating intricate multiphase flows characterized by distinct phase boundaries that necessitate precise tracking.

The characterization of phase distribution and interface positioning revolves around the fields of phase volume fraction, denoted as a_i.

$$a_i = \frac{V_i}{V} \tag{1}$$

where V_i is the volume of phase i in the cell and V is the volume of the cell. The volume fractions of all phases in a cell must sum up to one, In this paper, $a_{air} + a_{water} = 1$.

The distribution of phase i is driven by the phase mass conservation equation:

$$\frac{\partial}{\partial t}\int_V a_i dV + \oint_A a_i \mathbf{v} \cdot d\mathbf{a} = \int_V \left(S_{a_i} - \frac{a_i}{\rho_i}\frac{D_{\rho_i}}{D_t}\right) dV - \int_V \frac{1}{\rho_i} \nabla \cdot \left(a_i \rho_i \mathrm{v}_{d,i}\right) dV \tag{2}$$

where $\mathbf{a}$ represents the surface area vector, $\mathbf{v}$ is the mixture velocity, $\mathrm{v}_{d,i}$ stands for the diffusion velocity, S_{a_i} is a user-defined source term of phase i, and $\frac{D_{\rho_i}}{D_t}$ is the material of the phase densities ρ_i.

In this paper, VOF wave model is used to simulate surface gravity waves on an air and water interface and wave impact on floating platform.

A fifth-order wave is simulated using a fifth-order approximation based on the Stokes theory of waves. The characteristics of this wave, including its profile and phase velocity, are intricately linked to factors such as water depth, wave height, and the prevailing current.

The fifth order VOF waves are based on work by Fenton [49]. The Ursell number U_R is defined as:

$$U_R = \frac{\mathrm{H}\lambda^2}{d^3} \tag{3}$$

where H is the wave height, λ is the wavelength and d is the depth of the water.

To avoid wave reflection at the boundary affecting the floating body, this phenomenon can be effectively avoided by introducing vertical damping [50], which creates vertical resistance to the vertical motion of the wave.

$$S_z^d = \rho(f_1 + f_2|\omega|)\frac{e^{\kappa} - 1}{e^1 - 1}\omega \tag{4}$$

$$\kappa = \left(\frac{x - x_{sd}}{x_{ed} - x_{xd}}\right)^{n_d} \tag{5}$$

where x_{sd} represents initiation point for wave damping during propagation in the x-direction, x_{ed} is the end point of wave damping boundary, f_1, f_2 and n_d are parameters of the damping model, ω is the vertical velocity component.

2.3. Mooring modelling

The floating VAWT undergoes structural deformation under wind loads and hydrodynamic pressure loads [51]. In this paper, ABAQUS, a finite element analysis software developed by Dassault Systemes, is used to simulate and analyze the nonlinear dynamic response of the structure. Implicit direct-integration dynamic analysis is used to study nonlinear transient dynamic response of floating structure in Abaqus/Standard.

AQUA as a submodule of ABAQUS is designed to simulate hydro-elastic responses in flexible structures that are either submerged or partially submerged. This submodule proves especially valuable for analyzing scenarios involving components such as pipelines, risers, and mooring lines situated underwater.

The catenaries are simulated as hybrid beam element, the transverse drag force, tangential drag force and inertia force per unit length on the element are:

$$F_D = \frac{1}{2}\rho C_D D \Delta\mathbf{v}_n (\Delta\mathbf{v}_n \cdot \mathbf{v}_n)^{\frac{1}{2}} \tag{6}$$

$$F_T = \frac{1}{2}\rho C_T \pi D \Delta\mathbf{v}_t |\Delta\mathbf{v}_t|^{h-1} \tag{7}$$

$$F_I = \frac{1}{4}\rho \pi D^2 \left[C_M\left(\mathbf{a}_f - \mathbf{a}_f \cdot \mathbf{tt}\right) + C_A\left(\mathbf{a}_p - \mathbf{a}_p \cdot \mathbf{tt}\right)\right] \tag{8}$$

where ρ is the fluid density, C_D, C_T, C_M and C_A are the transverse drag coefficient, tangential (axial) drag coefficient, transverse inertia coefficient and transverse added-mass coefficient respectively, $\Delta\mathbf{v}_n = \Delta\mathbf{v} - \Delta\mathbf{v}_t$ represents the relative transverse velocity of the fluid, $\Delta\mathbf{v}_t = (\Delta\mathbf{v}\cdot\mathbf{t})\mathbf{t}$ is the relative tangential (axial) velocity of the fluid, $\mathbf{a}_f$ is the fluid particle acceleration, $\mathbf{a}_p$ is the acceleration of a point on the element, h is the exponent for tangential drag.

3. Model description

3.1. Geometry Model

The research object of this paper is a three-bladed H-type VAWT, as shown in Fig. 3. The geometrical model design refers to the 5 MW offshore VAWT design proposed by Hand et al [52], The main difference with Hand's model is that a smaller VAWT rotor size and the number of blades increased to three are used in this paper by considering platform buoyancy, load-bearing capacity, and stability. The geometry features are detailed in Table 2.

The VAWT tower, support rods and blades are modeled as shells. The connecting rods are swept using NACA airfoils of different thicknesses, and the internal arrangement of five shear webs extends consistently from the root of the tower to the blade joints, while the blades only have two shear webs placed at 15% and 50% of the chord length. To enhance the overall stability of the structure, the first and third shear webs of the support struts are connected to the shear webs of the blades at their ends, see the shear webs marked in brown color in Fig. 3.

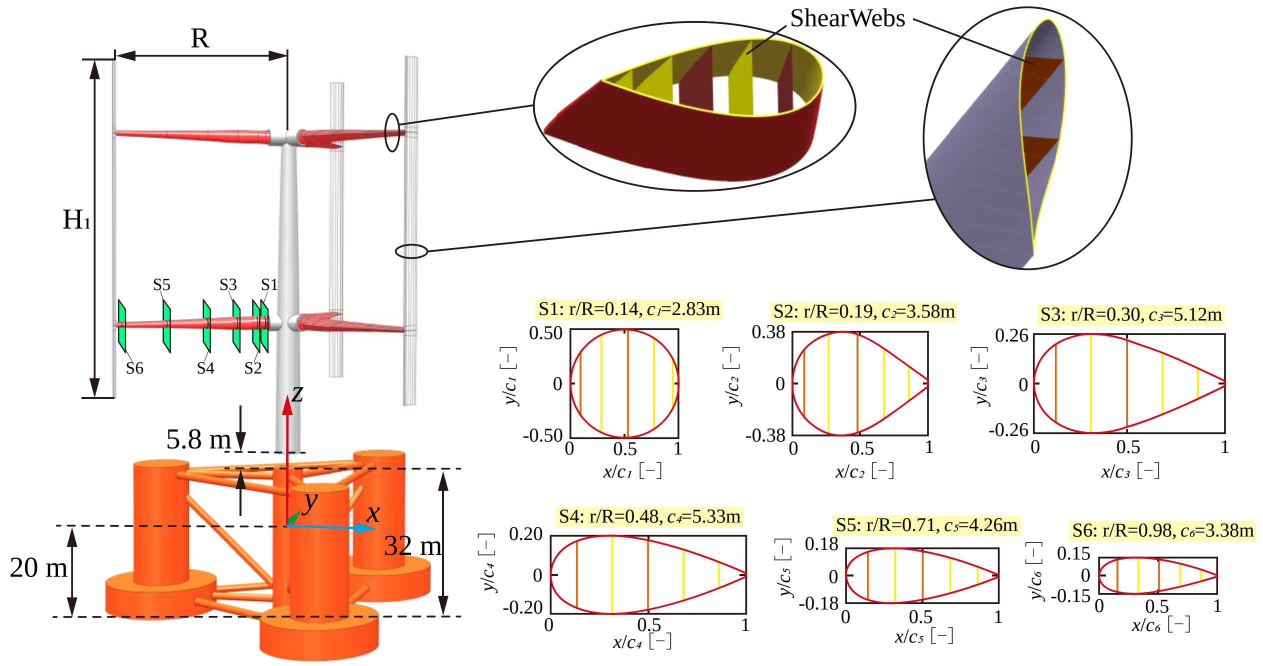

Fig. 3 Geometry model of floating VAWT.

Table 2 – Geometrical and operational parameters of floating VAWT

Characteristic	Specification
Blade airfoil	DU-06-W-200
Number of blades [N]	3
Connecting rods per Blade [N]	2
Height of blade, H_1 [m]	70.25
Tower Height, H_2 [m]	68.29
Radius, R [m]	36.76
Chord, c [m]	3.512
Blade pitch angle, β [°]	2
Rotor Speed, ω [rpm]	6.81
Optimal tip sped ratio (TSR)	3.28

The OC4 semi-submersible floating platform (geometric parameters detailed in Ref. [53]) is adapted to support the present VAWT, which was initially designed to provide support for the NREL (National Renewable Energy Laboratory) 5 MW offshore HAWT design.

3.2. Material properties

3.2.1. VAWT

Composites are used as material for VAWT blades due to their good mechanical properties, light weight and corrosion resistance. According to the guidelines of provided by Hand et al. [54], the composites used in this paper consist of different materials including gelcoat, Nexut, core, unidirectional (UD) and bi-directional cross-ply (BIAX). The distribution of composite on the blade surface is shown in Fig. 4.

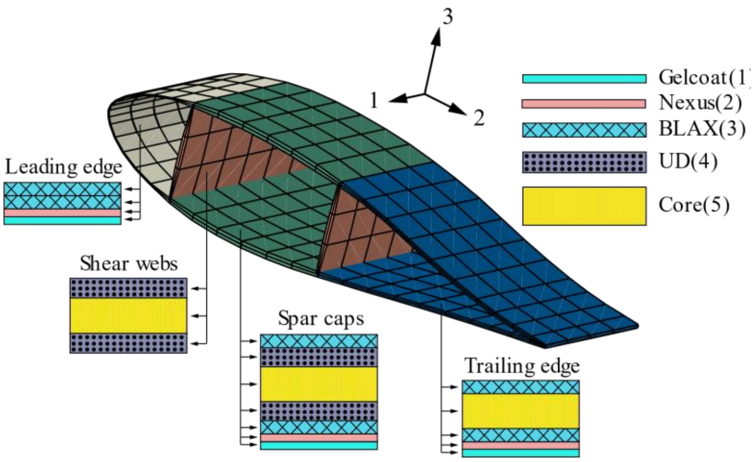

Fig. 4 The blade material layout for floating VAWT.

Nexus is an absorbent material used to apply Gelcoat. One layer of Nexut and Gelcoat is applied to all areas except the web. The specific layup parameters are shown in Table 3. Specific material properties can be obtained from Ref. [54].

Table 3 - Stack usage (ID) in each part of blade section.

Section	**Leading edge**	**Spar cap**			**Trailing edge**		**Shear webs**	
Stack ID	1,2,3	1,2,3,4,5,4,3			1,2,3,5,3		4,5,4	
Material	BIAX	BIAX	UD	Core	BIAX	Core	UD	Core
Number of plies	15	8	18	5	8	5	18	5

According to the above composite layup scheme, the total mass of the blade is 38,768.57 kg. The VAWT blade will be subjected to rotational centrifugal force load and wind load during the rotation process. In order to prevent large flutter deformation, the tower and the support arms are made of steel structure with a density of 8,500 kg/m^3, of which the thickness of the tower is 0.1m and the thickness of the support shaft is 0.01m, which gives the total weight of the VAWT of 11,842,435 kg.

3.2.2. Floating platform

The offset columns of floating semi-submersible platform are filled with ballast water to ensure that the platform has a lower center of gravity to ensure that it does not overturn in complex marine environments. During the initial geometric modeling process, the platform geometric parameters and the thickness of each component are consistent with Ref. [53]. The whole platform is made of steel with a density of 7850 kg/m^3 and a Young's modulus of 2.1×10^{11} Pa. The ballast water is modeled as a three-dimensional solid cell with a density of 1025 kg/m3, and some parameters related to the mass are shown in Table 4.

Table 4 - Comparison of initial platform design parameters with literature values

Parameter	Value in Ref. [53]	Value in CAE model	Deviation
Platform mass (including ballast)	1.3473×10^7 kg	1.3473×10^7 kg	0.0%
CM below SWL	13.46 m	13.46 m	0.0%
Moment of inertia about the CM (I_{xx})	6.827×10^9 kg·m^2	6.56×10^9 kg·m^2	-3.9%

Moment of inertia about the CM (I_{yy})	6.827×10^9 kg·m^2	6.56×10^9 kg·m^2	-3.9%
Moment of inertia about the CM (I_{zz})	1.226×10^{10} kg·m^2	1.17×10^{10} kg·m^2	-4.6%
Depth of ballast in upper columns	7.83 m	7.83 m	0.0%
Depth of ballast in base columns	5.0478 m	5.0478 m	0.0%
Total mass of ballast water	9.6208×10^6 kg	9.6208×10^6 kg	0.0%

In comparison to a floating 5 MW HAWT, a floating VAWT with similar scale blades will require more materials due to the inclusion of four additional connecting rods that link the tower to the blades. These rods play a crucial role in supporting and stabilizing the VAWT structure.

Therefore, it is necessary to adjust the depth of the ballast water, and properly adjust the thickness of each component of the platform (all adjusted to 0.06 m in this paper) in order to achieve a comparable draft to the original design and ensure that the structure does not produce a significant distortion. The specific parameters after adjustment are shown in Table 5.

Table 5 - Parameters related to platform mass after adjustment of ballast water and platform component thicknesses.

Parameter	Value
Platform mass (including ballast)	1.327×10^7 kg
CM below SWL	13.54 m
Depth of ballast water in upper columns	1.23 m
Depth of ballast water in base columns	5.88 m
Moment of inertia about the CM (I_{xx})	6.42×10^9 kg·m^2
Moment of inertia about the CM (I_{yy})	6.42×10^9 kg·m^2
Moment of inertia about the CM (I_{zz})	1.11×10^9 kg·m^2

3.2.3. Mooring lines

To ensure the stability of the floating platform, a mooring configuration involving three catenary lines is employed. In this study, a finite element method is employed to simulate the dynamic response of the mooring system. The contact between the mooring lines and seabed is considered. The equivalent material properties are detailed in Table 6.

Table 6 - Material properties of mooring lines.

Parameter	Value
Number of mooring lines	3
Unstretched length	835.5 m
Diameter	0.0766 m
Mass density	24596.55 kg
Young's modulus	1.367×10^{14}
Poisson's ratio	0.3
Seabed tangential friction coefficient, taken from Ref. [55]	0.74
Hydrodynamic transverse drag coefficient C_D	1.1
Transverse fluid inertia coefficient C_M	1.0
Transverse added-mass coefficient C_A	1.0

3.3. Fully coupled framework

The fully coupled model established in this paper is shown in Fig. 5. The computational process is conduct based on co-simulation of STAR-CCM+ and ABAQUS. The multiphase flow model in STAR-CCM+ considers the two-phase fluid containing air and water and generates the regular wave (7.58 wave height and 12.1 wave period) through the VOF wave model to investigate the aero-hydrodynamic response of the floating VAWT. The finite element structure containing rotor, platform, catenary and seabed is then considered in ABAQUS.

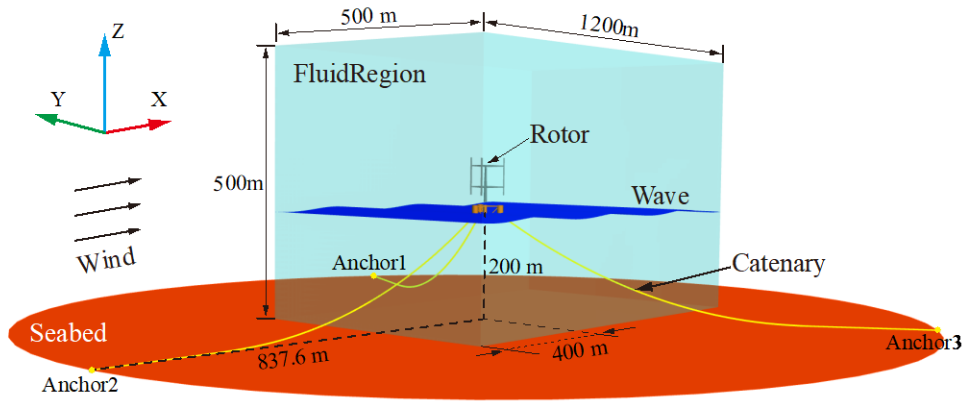

Fig. 5 Illustration of the fully coupled model for floating VAWT.

The specific computational flow is shown in Fig. 6, where the fluid loads, including wind pressure and wall shear stress, wave forces and buoyancy, are considered in STAR-CCM+ and transferred to the ABAQUS FEM model through the SIMULIA Co-Simulation Engine [56]. The platform's response to fluid loads generates a 6-DOF displacement. The catenary is subjected to inertial drag, lateral drag, and buoyancy forces in the AQUA module, and a restoring force is provided to the platform for it to move to the equilibrium position. The blades of the VAWT rotate at a constant angular velocity of 6.81 rpm, following the motion of the platform, resulting in a 7-DOF motion.

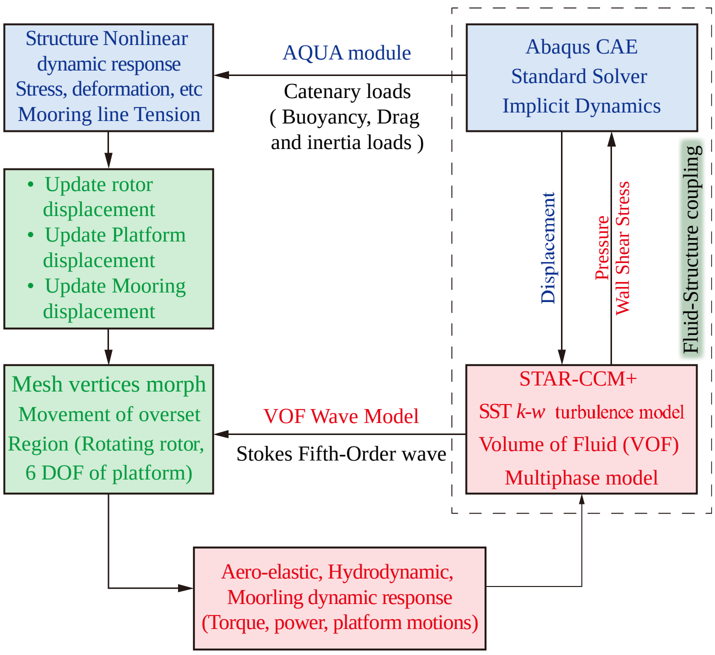

Fig. 6 The simulation process of fully coupled model.

The fully coupled computation was conducted on Prospero, a high-performance computing facility for research at Liverpool John Moores University (LJMU), which is equipped with 52 standard nodes, 2 memory-rich nodes and 1 GPU-accelerated node, providing a total of 3,536 cores. Simulations were performed simultaneously in STAR-CCM+ and ABAQUS/Standard, taking approximately 332 hours to complete 720,000 iterations using 256 cores.

4. Numerical setting and verification

The fully coupled floating VAWT model is a complex system, hence, it is important to verify its accuracy and reliability. Since there are no relevant experimental test results available at present, the verification part of this paper is preformed through three independent parts: turbulence model and grid independence, hydrodynamic free decay tests and finite element mesh validation.

4.1. CFD model and verification

4.1.1. Turbulence model

An H-type VAWT wind tunnel experiment (Fig. 7a) is used to verify the reliability of the turbulence model adopted in this paper. This experiment was recently conducted by Battisti et al. [57] to provide an experimental benchmark for researchers to assess the accuracy of the numerical code. The experiment utilized a large-scale, low turbulence wind tunnel at the Politecnico di Milano, testing two types of rotors (H-shaped and Troposkien) with detailed measurements of rotor torque, aerodynamic thrusts, and other performance parameters using specialized instrumentation.

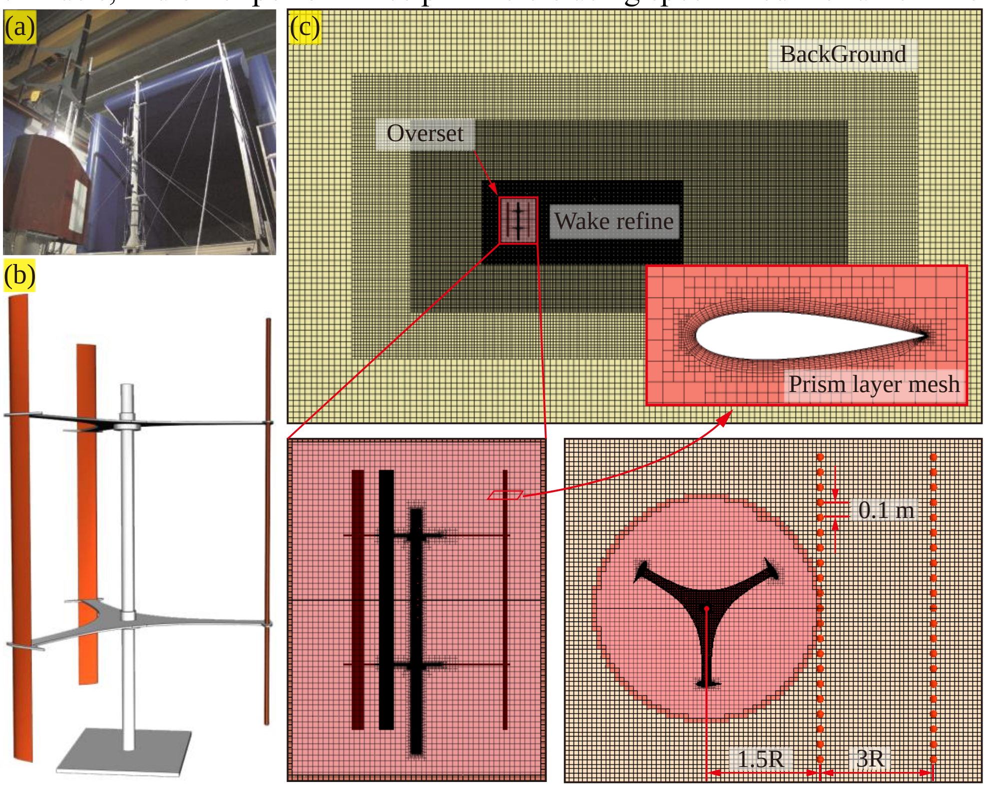

Fig. 7 The wind tunnel model and corresponding physical simulation flow domain: (a) wind tunnel model; (b) geometric model corresponding to wind tunnel experiment; (c) computational grid and boundary condition.

Fig. 7b shows the geometrical model used for numerical calculations: the geometrical parameters are highly consistent with the experimental model. Fig. 8c shows the generated grids and the distribution of wake velocity monitoring points in the mid-section of the VAWT, which are used for the subsequent verification of the wake velocity. The total grid number is 8531827, obtained by the structured hexahedral mesh generator in the STAR-CCM+. The turbulence model SST k-ω is used for the boundary layer development and fluid prediction of the reverse pressure gradient around the blades with a time step of 2.08×10^{-4} corresponding to a rotation of the rotor of 0.5 deg per time step.

Fig. 8 shows that the time-averaged power coefficients (Eq. (9)) and the experimental values are in excellent agreement over the entire range of TSRs, with deviations only at TSR > 3.3.

$$C_p = \frac{Power}{0.5 \cdot \rho \cdot A \cdot U^3} \tag{9}$$

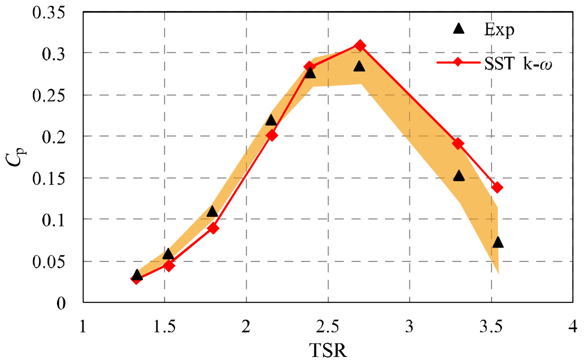

Fig. 8 Comparison of power coefficients with experimental values

Fig. 9 shows the comparison of the wake velocity with the experimental values at two positions of x/D = 0.75 and x/D = 1.5 downstream of the mid-section in the VAWT. A very good agreement is again achieved across different TSRs. The observed deviations are due to the inherent limitations of the RANS-based model, which fails to capture turbulent flows involving stronger turbulent eddies and unsteady effects. Overall, the SST k-ω model is able to provide reasonable results after weighing the numerical accuracy and computational resources.

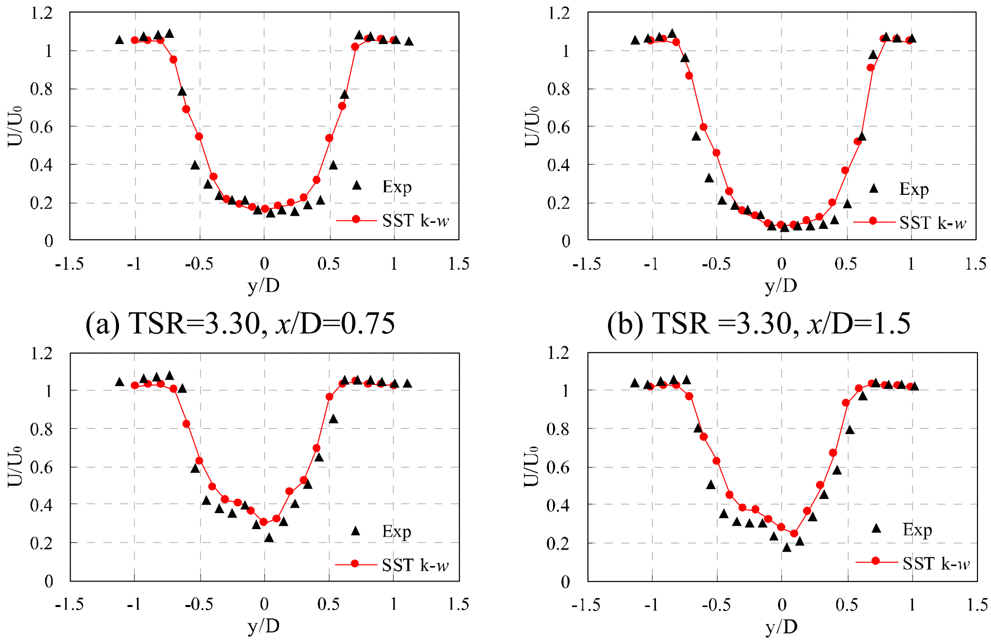

(a) TSR=3.30, *x*/D=0.75 (b) TSR =3.30, *x*/D=1.5

(c) TSR =2.40, *x*/D=0.75 (d) TSR =2.40, *x*/D=1.5

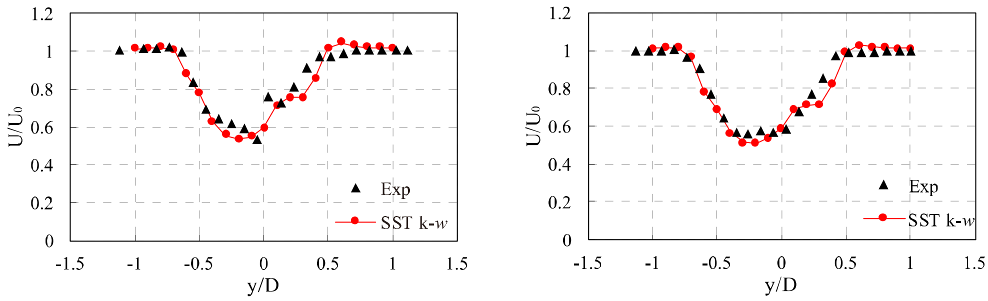

(e) TSR =1.80, *x*/D=0.75 (f) TSR =1.80, *x*/D=1.5

Fig. 9 Comparison of wake velocity at the mid-section of the rotor with experimental values for different TSRs

4.1.2. Grid sensitivity analysis

The computational grid for the floating VAWT is shown in Fig. 10. The overlapping grid technique is used to manage the rotor rotation and the 6-DOF motion of the platform. The “morphing” strategy is applied to calculate the structural deformation in regions Z1 and Z3, where the rotor and platform are located. The grid at the air-water interface is refined to enhance the tracking of the fluid dynamics altered by the floating platform using the VOF multiphase flow model, which facilitates real-time updating of the spatial distribution of the air-water two-phase flow. The entire domain is configured as an orthogonal trimmed mesh.

The refinement region in the background region uses a grid size of 5 m. Uniform grid sizes of 1.25 m are maintained at the air-water interface, the rotor wake region, and the rotation zone to ensure effective implementation of overlapping grid motions. The prism layer mesh in the simulations is configured using the SST k-ω turbulence model with the "all y+ wall treatment" option in STAR-CCM+. Twelve prismatic layers are employed near the blade surface, with a near-wall thickness of 0.001 m, a total boundary layer thickness of 0.3 m, and a growth rate of 1.2. Adjustments to the dimensions of the blade wake and the airfoil surface enable the computation of power coefficients C_p at three different mesh scales, as detailed in Table 7. These calculations are performed under an optimal TSR of 3.28, with a free stream velocity of 8 m/s and a time step of 0.01 s. The initial turbulence intensity at the inlet of the computational domain is set to 1%. The solution is considered to have converged when the residuals for relevant quantities (including Tke, Sdr, and momentum) approach 10^{-4}, and the variation in the torque coefficient for VAWT between two consecutive revolutions is less than 1%.

It is important to note that the sensitivity analysis does not consider the platform motion and the fluid-structure coupling effects. The CAE solver was frozen to save computational resources, focusing solely on the rotation of the VAWT at a prescribed speed of 6.81 rpm.

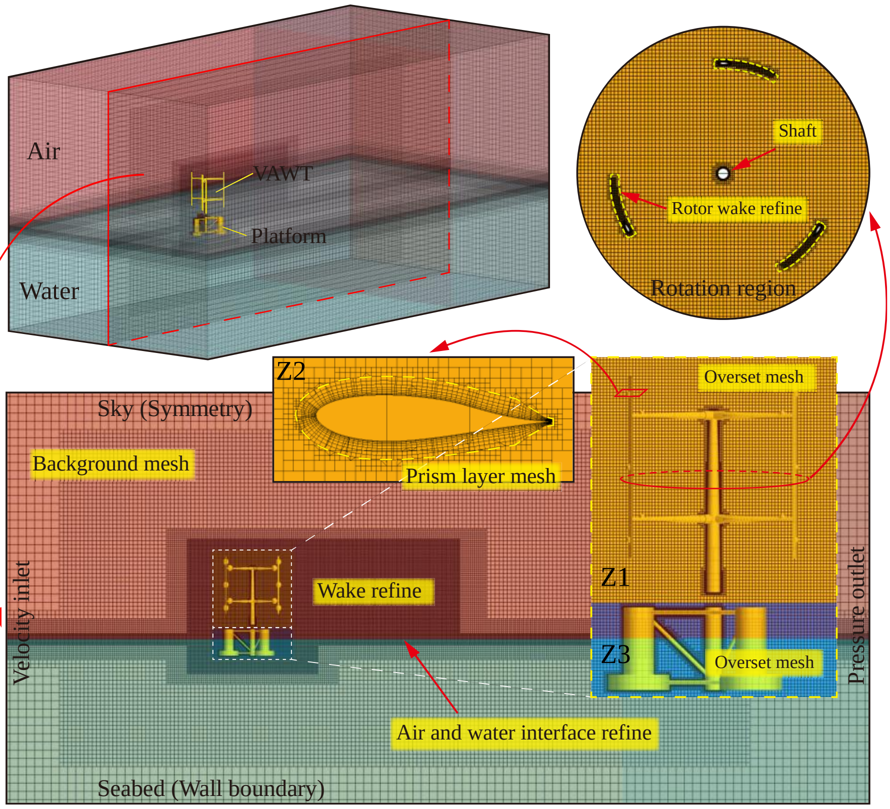

Fig. 10 The grid distribution of floating VAWT

As shown in Table 7, the difference in the C_p values calculated using Grid2 relative to Grid3 is only 0.77%. This minimal discrepancy suggests that further refinement of the grid would not significantly improve the results. Consequently, the Grid2 has been chosen for subsequent fully coupled simulations of the floating VAWT.

Table 7 - Power coefficient of floating VAWT with different grid size

Description	Grid1	Grid2	Grid3
The size of blade wake (Z2)	0.63	0.31	0.16
The size of airfoil	0.075	0.054	0.033
Cells in rotation region (Z1)	6101630	11016308	14424570
Total cells	16321930	20252332	24644224
C_p	0.3032	0.3123	0.3147

4.2. Hydrodynamic part verification

The free decay test is employed to validate the hydrodynamic aspects of this paper. This is achieved by releasing the platform freely from a predetermined initial position. In this study, the fully coupled method mentioned in Section 3.3 is used to compute the free decay response of the semi-submersible platform (Fig. 11). On the structural side, the rotor, nacelle, platform, mooring, and seabed are all taken into consideration. To conserve computational resources, the original HAWT blades and nacelle have been simplified to an equivalent concentrated mass (ECM) located at the top of the tower, and they are modelled as 3D solid cells in the FEM model. Wind loads are not considered on the fluid side, and a flat VOF wave is employed to simulate the hydrodynamic response of the platform in calm water.

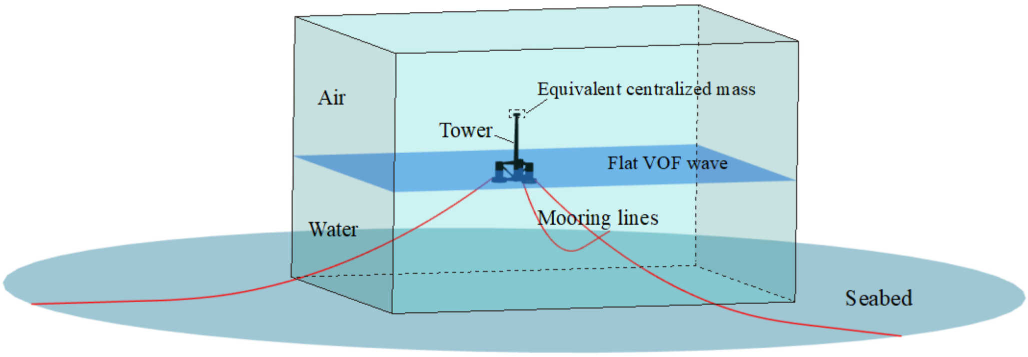

Fig. 11 The free decay test of a floating platform with equivalent components

Table 8 provides a comprehensive overview of the mass-related structural properties of the free decay model developed in this study. These properties are then compared with data from the 5MW semi-submersible floating HAWT in Ref. [58], revealing that the disparities are negligible. As a result, this model can be considered equivalent and suitable for validating the hydrodynamic part presented in this paper.

Table 8 Mass-related properties of floating platforms with equivalent components.

	Mass in FEA model (kg)	Deviation with Ref. [58]	CM Location in FEA model (m)	Deviation with Ref. [58]
Tower	249718.03	0.007%	44.3	2.1%
Platform	13473097.00	0.023%	-13.46	0.0%
ECM (Rotor and nacelle)	350061.81	0.018%	87.6	0.0%
Total	14072876.00	0.020%	-9.84	0.98%

The calculated surge and pitch responses were compared with those calculated by NREL FAST V8.1 and Tran et al [17] using the same numerical code STAR-CCM+ as shown in Fig. 12.

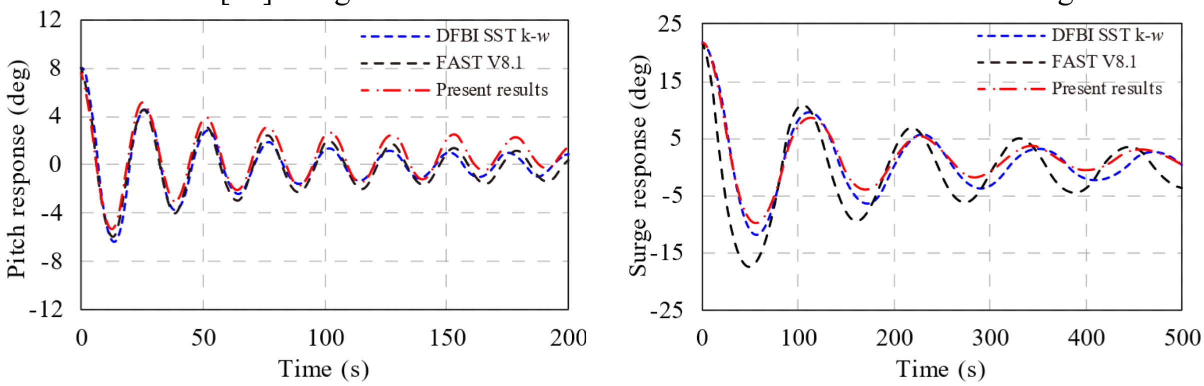

(a) Pitch free decay response (b) Surge free decay response

Fig. 12 Comparison of the free-decay tests of different numerical code.

The trends of the decay responses of the platform computed by these three different methods are in good agreement, differing only in phase and amplitude (Fig. 12). The difference between the present approach and Tran et al's [17], who used the DFBI method integrated in the STAR-CCM+, is that they did not consider the actual structural properties. The mass-related properties were predefined directly on the platform. In addition, a quasi-static method was used to simulate the moorings, which may cause inaccuracies in the mooring tension restoring moment.

In contrast, the surge and pitch responses calculated in this paper using the fully coupled model can reach the equilibrium position faster after free release. This is partly because the contact friction effect between the mooring and the seabed, and of the transverse inertial drag and buoyancy of the mooring were considered. This made it possible for moorings to reach the steady state faster. Overall, the calculated values of each code are in good agreement, which proves the reliability and reasonableness of the coupled model in this paper.

4.3. FEM model and verification

The FEM mesh of the floating VAWT is shown in Fig. 13. The rotor, tower, platform, and seabed components are represented as 3D shell elements, while the mooring lines are modelled as 3D beam elements. Details of the element types and the corresponding number can be found in Table 9.

Table 9 – Element type and number for floating VAWT.

	Rotor	Ballast	Platform	Catenary	Seabed
Element type	S4R	C3D8R	S4R	B31	S4R
Element number	79110	3894	15978	2508	319

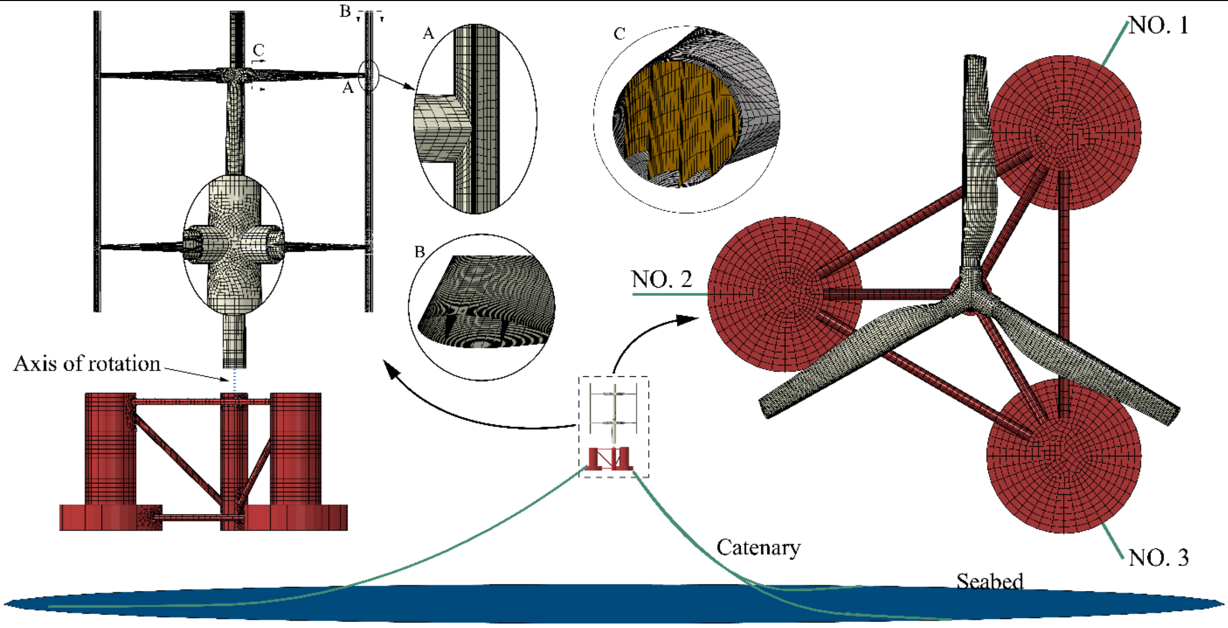

Fig. 13 The FEM mesh for Floating VAWT

The Floating VAWT was connected to the floating platform using a "Hinge" connector in ABAQUS, facilitating the transfer of thrust and vibrations from the blades and arms to the platform. To simulate the VAWT rotation, a reference point was created at the center of the tower base, with a coupling constraint linking its rotation to the turbine blades. A rotational boundary condition was applied, allowing the VAWT to uniformly accelerate from zero to the rated speed of 6.81 rpm.

Similar to CFD modelling, mesh independence must be verified for the finite element mesh. Given that blades experience significantly more deformation during operation compared to other components, our mesh independence assessment focused specifically on the blades. This validation ensures that the blades accurately and precisely capture the fluid loads.

The extreme wind load of 70 m/s (taken from IEC 61400-01 [59], a standard that defines 50 years of extreme wind conditions as one of the most critical loading scenarios for wind turbine in parked condition) is mapped onto a single blade within STAR-CCM+. The deformation of the blade with different element sizes is analyzed using a static analysis method in ABAQUS. The coupling steps are shown in Fig. 14.

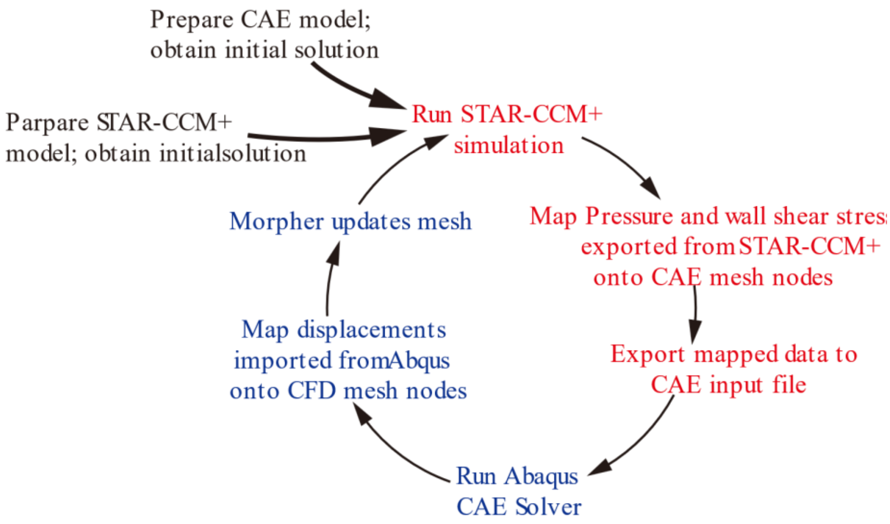

Fig. 14 The mapping steps of wind load

The blade CAE model was imported into STAR-CCM+ to calculate the pressure and wall shear stresses at the fluid-structure interface. These data were then used to define the traction loads on the FSI surfaces in the CAE model, and the resulting displacements were subsequently calculated using ABAQUS, as shown in Fig. 15.

The maximum and minimum deformation locations for different aspect ratios (1: 2, 1: 1.5, and 1:1) are basically the same. The maximum deformation location occurs at the tip of the blade, which may be due to the strong vortex shedding in this region. As the cell size decreases from 1:2 to 1:1.5, the maximum deformation value decreases marginally from 2.84 to 2.838. Further reduction in cell size from 1:1.5 to 1:1 does not significantly alter the overall deformation distribution. Consequently, a cell size of 1:1.5 is selected for subsequent structural calculations, balancing the computational resources and accuracy required.

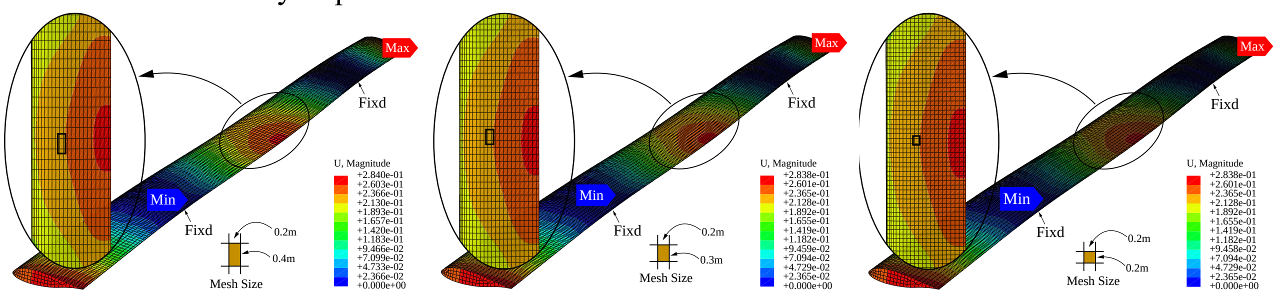

Fig. 15 The structure response of VAWT blades with different mesh sizes

5. Results and discussion

In this section, the proposed fully coupled model is employed to conduct two-way fluid-structure interaction analysis on floating VAWTs. The aerodynamic performance, hydrodynamic response and structural nonlinearities are investigated.

5.1. Analysis of unsteady aerodynamics

5.1.1. Power and flow field

The rotor motion in a floating VAWT differs significantly from that in a fixed VAWT. The reason being the dynamic interaction between the rotor and the floating platform under wave loading, which results in intricate, multi-dimensional movements that influence the performance and behavior of the rotor. Fig. 16 illustrates the time-domain curves of the power coefficients for the fixed and floating VAWT.

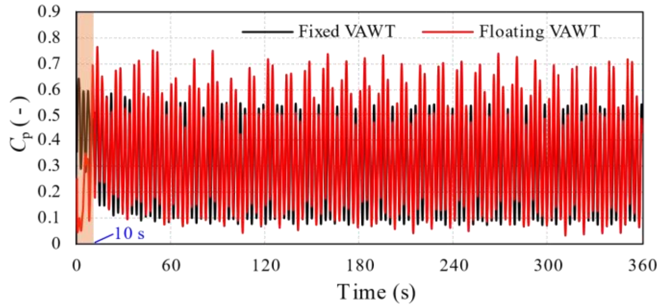

Fig. 16 Comparison of power coefficients between fixed and floating VAWTs

In Fig. 16, the power coefficient of the fixed VAWT exhibits significant consistency and predictability after time t > 120 s, with its C_p values fluctuating within the range of [0, 0.55]. In contrast, the floating VAWT demonstrates more severe fluctuations in power coefficients, featuring spike-like peaks that far exceed the maximum C_p values observed in the fixed VAWT. This is primarily due to the dynamic response of the platform altering the inflow conditions to the blades, particularly when the speed of the blades relative to the fluid adds to the ambient wind speed, with the result that the apparent wind experienced by the rotor is stronger and, consequently, the energy extraction of the VAWT is greater at certain times.

In addition, for t < 10 s, the difference between the power coefficients of floating and fixed VAWTs stems primarily from the different strategies adopted at startup. The fixed VAWT employs rigid blades and quickly reaches a set constant rotational speed upon startup. In contrast, the floating VAWT uses blades made of flexible composite materials. To avoid large structural deformations and potential computational instability due to rapid acceleration, its rotational speed gradually increases from zero to the rated speed over approximately 10 s, resulting in a progressively rising power coefficient trend.

After calculating the average power coefficient over the last 20 complete revolutions of stable operation, it was found that the C_p value for the floating VAWT was 0.341, which represents a 9.3% increase compared to the fixed VAWT (0.312). This result indicates that the floating VAWT is more efficient in converting wind energy into mechanical energy than the fixed-bottom VAWT.

To further investigate the physical mechanisms behind the higher power coefficient of the floating VAWT relative to the fixed VAWT, Fig. 17 displays a comparison of the instantaneous velocity and vorticity field contours for both the fixed and floating VAWTs.

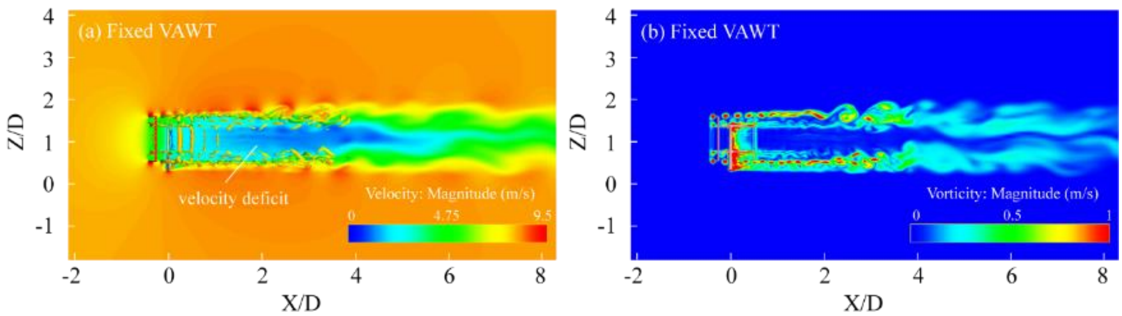

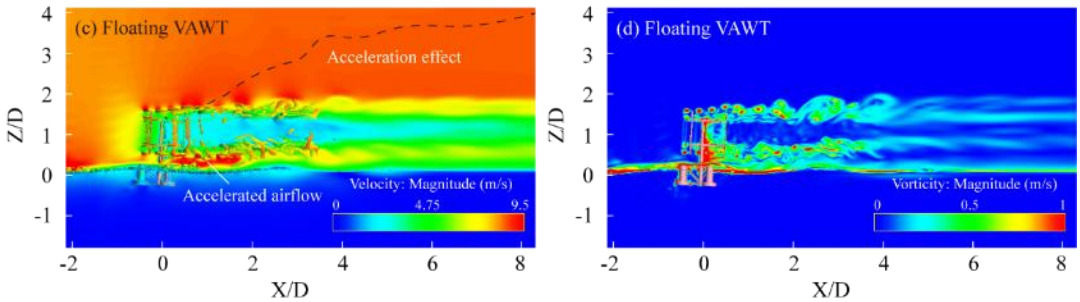

Fig. 17 Instantaneous velocity and vorticity field contours of floating and fixed VAWTs

In Fig. 17a and 17c, it is evident that there is a significant velocity deficit behind the fixed VAWT, within the area of 1≤X/D≤4. As the wake progresses further away to X/D=6, the velocity gradually recovers. In contrast, the wake of the floating VAWT dissipates more rapidly, with a lesser velocity deficit by X/D=4. Additionally, a distinct fluid acceleration effect is observed in the region above the wake, within 2≤Z/D≤4, which is attributed to the influence of platform motions. These motions facilitate the interaction between the rotor and the surrounding fluid, thereby imparting additional kinetic energy to the airflow. Particularly between the tower and the water surface, the narrow space resulting from the omission of the VAWT transmission apparatus leads to a significant channel acceleration phenomenon, causing the velocities in this area to be notably higher than those in surrounding regions.

As can be seen from Fig. 17b and 17d, it is evident that due to the stationary position of the fixed VAWT, distinct shedding vortices occur at the blade tips, with consistent vortex sizes and spacing. The blades rotating to the downwind region collide and interact with the vortices shed by the upstream blades. For the floating VAWT, the inclination of the platform forward and aft enables the downwind blades to evade the vortices shed from the upstream, further explaining why floating VAWTs exhibit a higher power coefficient compared to fixed VAWTs.

5.1.2. Wake characteristics

Fig. 18 illustrates the wake velocity contours at the mid-section (Z=66 m) of both fixed and floating VAWTs. By symmetrically arranging wake velocity monitoring points along the Y-direction at distances of 2D, 4D, 6D, and 8D from the rotating center of the rotor, the wake velocity distributions at different distances from the turbine center are obtained, as depicted in Fig. 19.

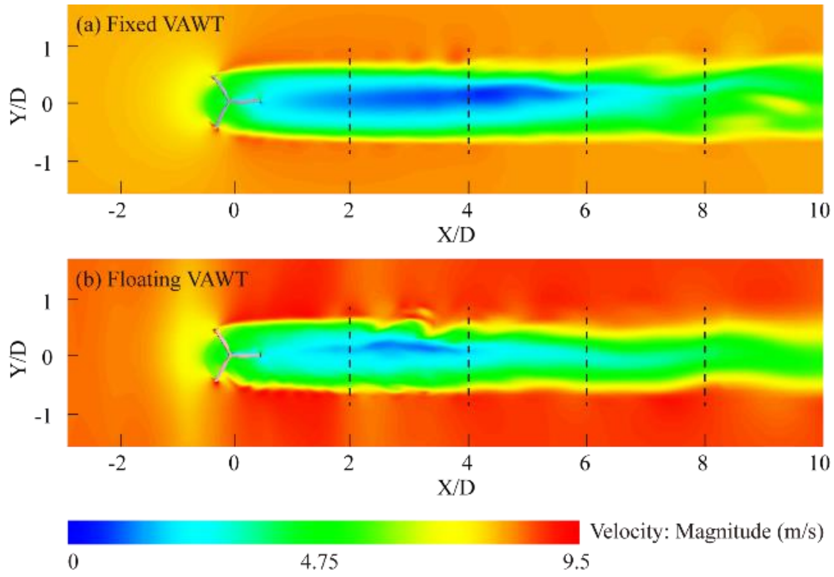

Fig. 18 Wake velocity distribution in the middle section of floating and fixed VAWT

As illustrated in Fig. 19, at X/D=2, the wake velocities of both fixed and floating VAWTs are symmetrically distributed along the centerline behind the turbine, with the lowest velocities observed in the central region, exhibiting a bowl-shaped. As the wake develops further downstream, the velocity curve gradually flattens and becomes irregular, indicating a progressive recovery of the VAWT wake.

Within the range of 2≤X/D≤6, the wake velocities of floating VAWTs are generally higher than those of fixed VAWTs. Especially when X/D=4 and 6, and in the region of 0≤Y/D≤0.8, the difference in wake velocities between the two types is more pronounced. This is primarily attributed to the inducing effect of fixed VAWTs on the surrounding fluid during rotation, causing the wake to tilt towards the positive Y direction.

At the position of X/D=6 and Y/D=0.2, the wake velocity of the floating VAWT increases significantly compared with the fixed VAWT, by approximately 171%. However, when X/D=8, the velocity of the wake centerline (Y/D=0) of the floating VAWT decreases slightly compared to the fixed VAWT. This is mainly due to the reciprocating motion of the floating platform, which increases the momentum of the low-speed fluid in the distant wake region. Therefore, the fluid velocity at the wake centerline maintains the upstream wake velocity over a relatively long distance.

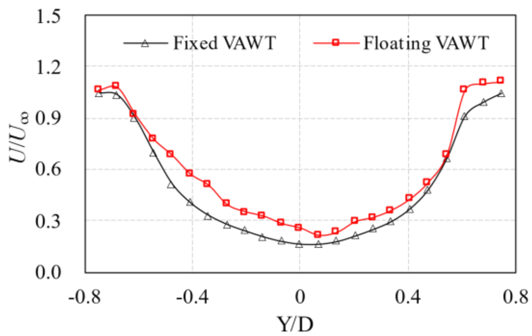

(a) X/D= 2

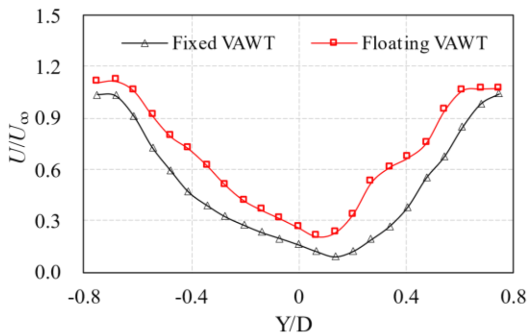

(b) X/D= 4

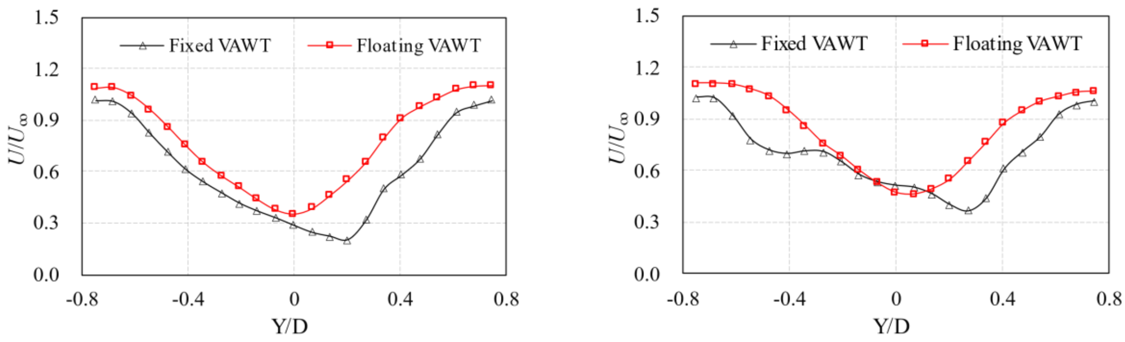

(c) X/D= 6 (d) X/D= 8

Fig.20 Comparison of wake velocities in the middle section of floating and fixed VAWTs

5.1.3. Correlation of blade torque with platform motion

To further investigate the connection between the platform responses and aerodynamic performance of floating VAWT, two complete wave periods, T_{wave}, corresponding to surge, pitch, and heave responses were selected for analysis. Additionally, the torque time-domain curves for single blade of both floating and fixed VAWTs over the same time span are examined in detail, as depicted in Fig. 20. The rotational periods for blades 1 (B1), blade2 (B2), and blade3 (B3) of the VAWT are denoted as T_i (i=1, 2, 3). A complete rotational period is defined when the blade azimuth angle changes from 0° to 360°, where the azimuth angle of 0° is defined as the position where the blade's leading edge is facing the wind direction, and the chord of the blade is parallel to the wind direction, thus T_i=0.

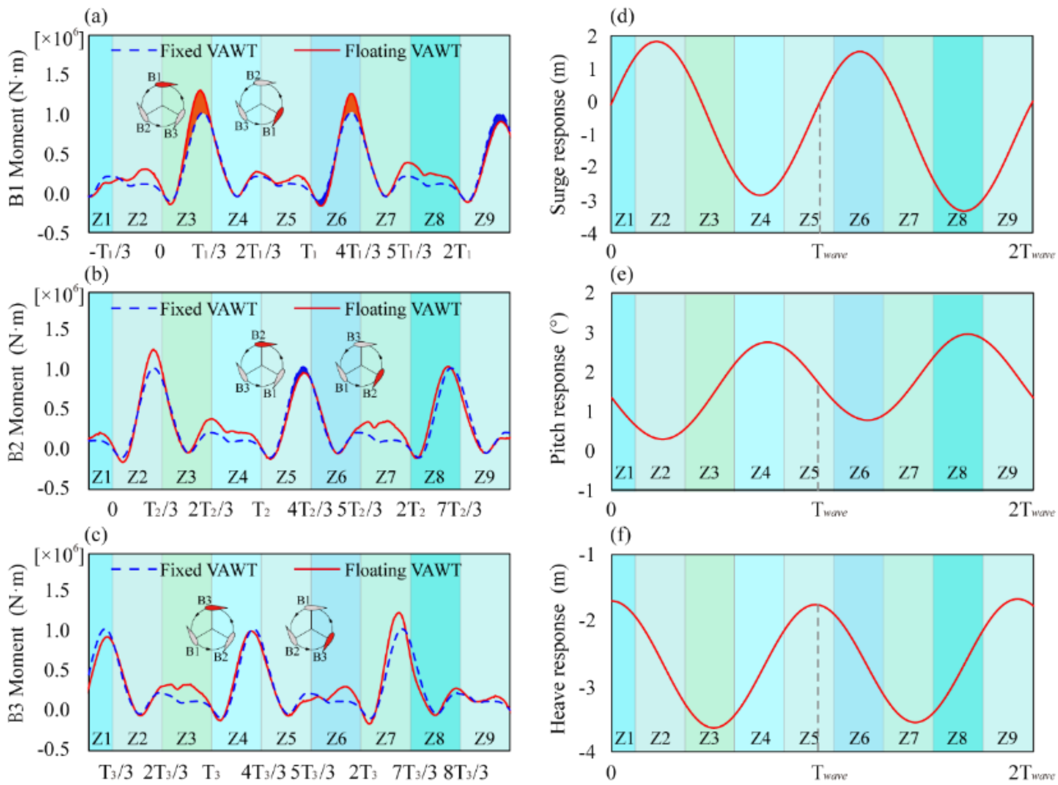

Fig. 20 Single blade torque of floating and fixed VAWT in two wave periods

In Fig 20a-c, it can first be observed that the azimuth difference of the torque curves for B1, B2 and B3 is 120° (Ti/3). This is due to the unique structural characteristics of the three-blade VAWT, where each blade occupies a different position and state of motion, spaced 120° apart in the rotor plane. The torque curve for each blade exhibits a distinct peak within the initial one-third of the rotation period (0 to $T_i/3$). This peak occurs as the blade rotates toward the windward side, where an increase in the effective angle of attack (AOA) leads to a continuous enhancement of the torque, typically reaching its maximum around $T_i/4$. Following this peak, the torque curve shows a more subdued fluctuation due to the blade having captured a substantial amount of energy on the windward side, which results in relatively reduced energy extraction in the leeward region. Further comparison of the torque curves between fixed and floating VAWTs reveals that neither type consistently exhibits absolute superiority throughout the entire rotation cycle; instead, their performance superiority alternates. Specifically, the floating VAWT exhibits higher torque output than the fixed VAWT during certain time intervals, while the opposite is true during other time intervals.

As shown in Fig. 20d-f, it is evident that there is a significant correlation between the surge and pitch responses of the floating platform and the torque curves of the VAWT blades within the azimuth angle of 0-120°, corresponding to the time intervals of [0 to $T_i/3$].

Taking the torque curve of B1 as an example, when the platform surges toward the negative X direction and the pitch angle increases (see Z3 in Fig. 20d and e), the peak torque of B1 for floating VAWT increases by 27.1% compared to the fixed VAWT (see Z3 in Fig. 20a); In contrast, when the platform surges toward the positive X direction and the pitch angle decreases (see Z9 in Fig. 20d and e), the peak torque of the floating VAWT blades decreases by 13.6% relative to the fixed VAWT. (see Z9 in Fig. 20a). Furthermore, as the floating platform transitions between peak and trough positions in its surge and pitch responses (see Z6 in Fig. 20d and e), the torque curve of the floating VAWT simultaneously exhibits characteristics that are both superior and inferior to those of the fixed VAWT (see Z6 in Fig. 20a).

However, when the azimuth angle of B1 is between 240-360°, corresponding to the time intervals [$2T_1/3$, T_1] and [$5T_1/3$, $2T_1$], there seems to be no direct correlation between its torque variation and the surge and pitch responses of platform. As observed from Z5 and Z8 in Fig. 20a, despite the floating platform surges toward the positive X direction (see Z5 in Fig. 20d) or being at the transition of the surge trough (see Z8 in Fig. 20d), the torque of B1 for the floating VAWT consistently exceeds that of the fixed VAWT. This increase in torque can be attributed to the tilting (pitch) and movement (surge and heave) of platform. As B1 rotates into the leeward region, it fortuitously avoids the upstream wake, consequently enhancing the torque.

In summary, three main aspects arise from the analysis above regarding the torque variation for floating VAWT blades in the rotation period of [0, Ti/3].

- When the surge direction of the floating platform is opposite to the wind direction, the velocity of the blade movement relative to the fluid and the incoming flow will produce a superimposing effect, thereby increasing the effective AOA of the blades on the floating VAWT compared to those on the fixed VAWT, ultimately increasing the torque (see Z7 in Fig. 20c).

  It should be noted that, the surge and pitch responses of the platform have the same period under regular wave, and they display opposite characteristics at the peak and trough. Therefore, when the platform surges toward the negative X direction, an increased pitch response of the platform (causing the rotor to tilt backward) will cause the blades on the windward side to move relatively backward, thus weakening this superimposing effect.
- When the surge direction of the floating platform aligns with the wind direction, the velocity of blade movement relative to the fluid and the incoming flow velocity would negate each other.

This results in a lower effective AOA for the blades on the floating VAWT compared to the fixed VAWT, ultimately leading to reduced torque (see Z5 in Fig. 20b). At this time, a decreased pitch response of the platform (causing the rotor to tilt forward) will cause the blades on the windward side to move relatively forward, thereby alleviating this negating effect.

- The increase in torque due to the superimposing effect is greater than the reduction in torque due to the negating effect. As can be seen from Z3 in Fig. 21a and Z5 in Fig. 20b, the floating platform undergoes surge motion toward the negative and positive X directions respectively. However, the increase in torque observed in the Z3 of Fig. 20a is significantly greater than the reduction in torque seen in the Z5 of Fig. 20b.

5.2. Analysis of hydrodynamic response

5.2.1. Dynamic responses of platform

Under the wind and wave coupling, the platform is subjected not only to wave forces but also to thrust forces generated by wind loads on the tower. These forces are transferred to the platform, inducing a dynamic response that causes the catenary to undergo cyclic stretching and relaxation. The catenary primarily exerts a restoring moment on the platform to ensure dynamic equilibrium between the platform and the upper VAWT.

In the fully coupled model, the catenaries are modeled as a series of hybrid beam elements, as shown in Fig. 21. This approach accounts for the elastic deformation of each element and the contact effects between the catenaries and the seabed. It enables accurate computation of the dynamic behavior under complex sea conditions.

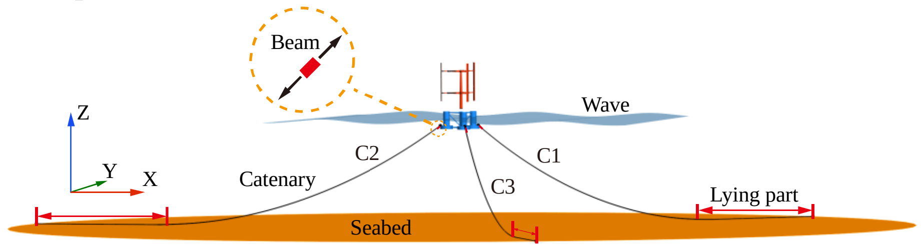

Fig. 21 Force diagram of the top beam element of the catenary for floating VAWT

Fig. 22 shows the dynamic response of the floating VAWT in six DOF under wind and wave loads. Fig. 22a-c reveal that the pitch response of the platform is significantly greater than the roll and yaw responses. This occurs mainly because when the wavelength is much larger than the platform's characteristic length, the wave direction has a strong effect on how much the platform tilts along the Y-axis, which makes the pitch more sensitive compared to the other two rotational DOF. The pitch amplitude for the floating VAWT ranges from 0 to 3 degrees, while the amplitudes of roll and yaw do not exceed 2 degrees, indicating they are negligible.

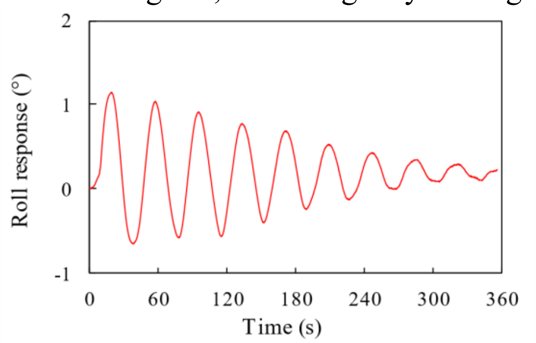

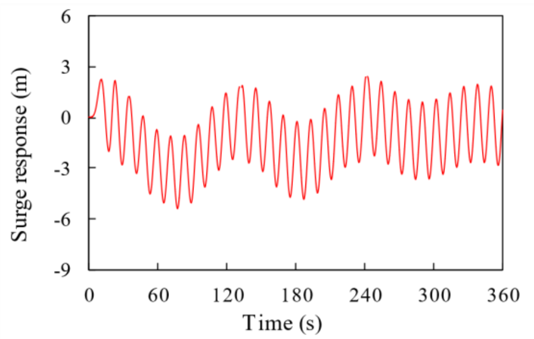

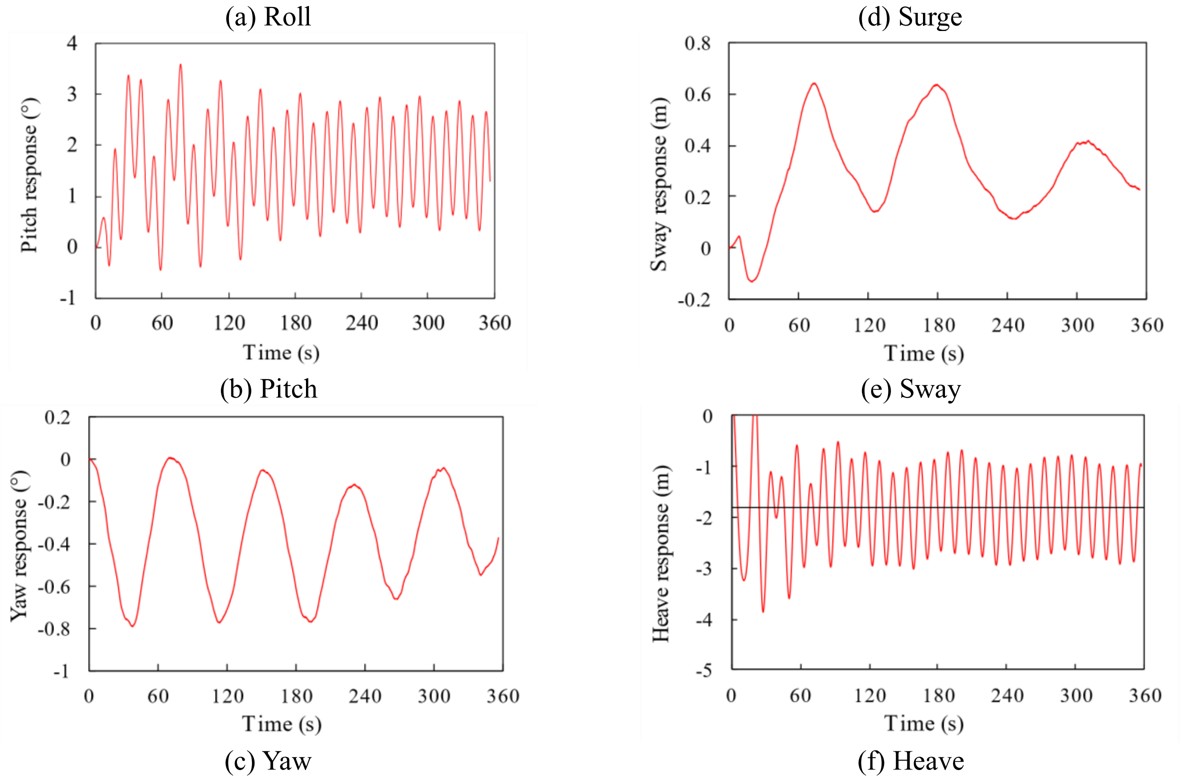

Fig. 22 Six degrees of freedom response of floating VAWT

As shown in Fig. 22d, the surge response of the floating VAWT is characterized by a left-right drift of its mean equilibrium position. Initially, for *t* <80 s, the platform's mean equilibrium position shifts towards the negative X direction due to the friction between the seabed and the lying part of the catenaries. The sudden impact of wave force causes catenary C2 to tighten abruptly, generating a significant restoring torque. Due to inertia effects, this leads to a mean equilibrium position of the platform in surge drifting towards the negative X direction. After that, the overall mean equilibrium position of the floating VAWT stabilizes and oscillates around X=0 m.

For the sway response (Fig. 22e), the fluctuation of the curve is less frequent, and more irregular compared to the other two translational DOF (surge and heave). It exhibits a slow, reciprocal drift along the Y-axis over an extended period, with a fluctuation amplitude ranging from [-0.2, 0.6] m.

During the initial 90 s simulation period, the heave response demonstrated significant instability with drastic fluctuation amplitudes (Fig. 22f). This is due to rebound effects caused by water resistance and inertial forces following the release of the floating VAWT in the fluid-structure coupling calculation. Furthermore, the heave response remained negative throughout the time range, oscillating around a mean equilibrium position of approximately -2.2 m along the Z-axis, indicating that the entire floating system has a deeper draft relative to the original waterline.

It should be noted that despite the adjustments to the ballast water in the OC4 semi-submersible platform in this study, the designed VAWT still results in an increased draft. The platform's buoyancy is slightly insufficient. Therefore, modifications to the platform or the addition of floats are necessary to maintain an optimal draft and ensure overall system stability.

5.2.2. Top tension of the catenary

Fig. 23 displays the time-varying tension curves of the catenaries (C1-C3) for the floating VAWT. Notably, the tension in C2 sharply increases within the first 8 s due to the impact of a sudden wave force. In addition, the friction between the catenaries and the seabed limits their range of motion, causing the floating system's mean equilibrium position in heave to shift toward the negative X-axis due to inertial forces. As a result, catenary C2 exhibits a greater state of relaxation compared to C1 and C3. Within a timeframe of less than 130 s, C2's tension is generally observed to be lower than that of C1 and C3. As the six DOF response of platform stabilizes, the tensions in all catenaries exhibit dynamic characteristics.

Further analysis shows that catenaries C1 and C3 have similar tension trends but different amplitudes. As tension in C2 increases, tensions in C1 and C3 decrease, and vice versa. This occurs because C2 is aligned with the wind-wave direction, while C1 and C3 are symmetrically positioned on either side, arranged in a 120° circle. Therefore, any lateral movement or tilting of the platform leads to an increase or decrease in tension on one side, which correspondingly affects the tensions on the opposite side.

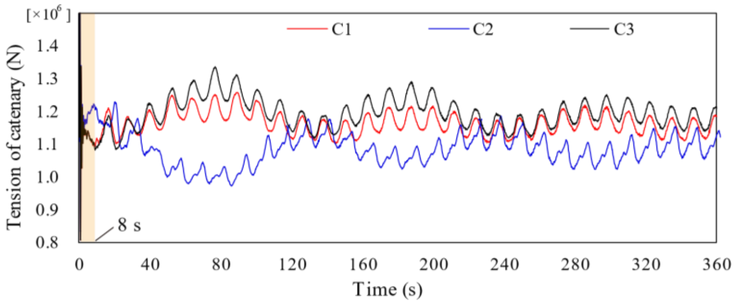

Fig.23 Top Tension of three catenary for floating VAWT

Fig. 24 reports the tension variations of C1-C3 across two wave periods. It can be observed that the tension in C2 increases with two distinct jumps. In conjunction with Fig. 20e and f, the first jump is due to an increase in the pitch angle, causing the whole system to tilt rightward. The second jump follows due to an increase in the heave response, as the platform moves upward along the Z-axis.

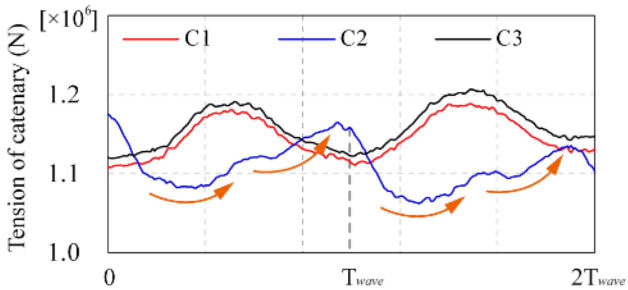

Fig. 24 Top Tension of three catenary for floating VAWT in two wave period

5.3. Analysis of structural nonlinearities

5.3.1. Structural stress and deformation

The structural nonlinear response of the floating VAWT involves complex interactions among its components. For the H-type VAWT, the blades are aligned parallel to the rotation axis and are positioned through arms connected to it, with the entire weight of the blades and arms supported by the tower. The VAWT is connected to the platform using a "Hinge" connector in ABAQUS, allowing the thrust caused by wind loads and the vibrations induced by deformations of the blades and arms to be transferred to the platform. The platform, affected by wave forces, generates a six DOF response that further influences the nonlinear structural effects of the VAWT.

Fig. 25 shows the structural stress and deformation of the floating VAWT. The highest stress in the floating VAWT (without shear webs) occurs at the bottom of the central pontoon of the platform (Fig. 25a), reaching about 3.228×10^8 Pa. This high stress is due to the central pontoon bearing the gravitational load of the entire tower and blades. The lowest stress appears at the upper tip of the blades, about 8.024×10^3 Pa. This is mainly because the blade tip area is far from the tower, arms, and other connection points, which are crucial areas in the VAWT for transferring forces and torques between components.

As can be seen from Fig. 25b, the maximum stress of shear webs occurs at the connection point between the arm and B3, reaching 6.281×10^8 Pa. This region is critical for structural optimization in engineering to prevent fatigue and damage. The lowest stress is found at the upper tip of B1's shear web, with a stress of 8.745×10^5 Pa.

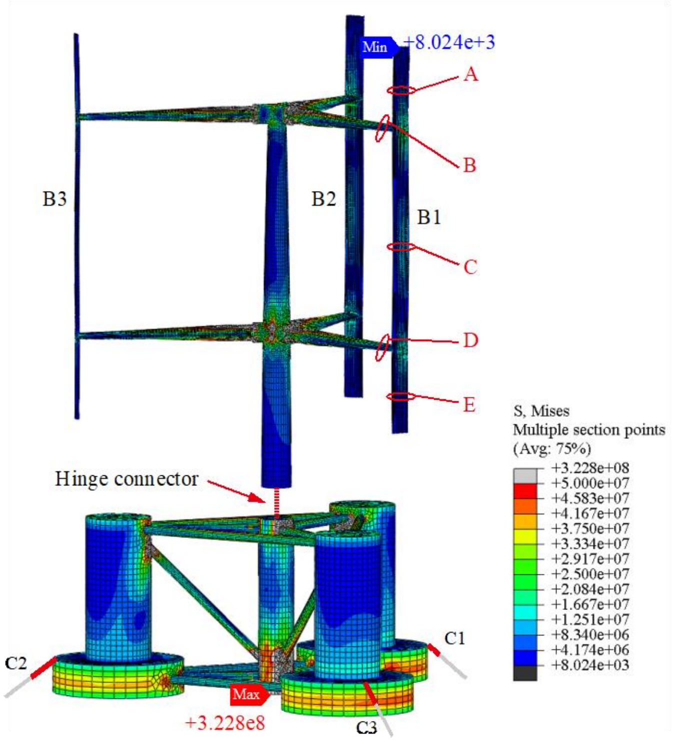

(a) Floating VAWT (without shear webs)

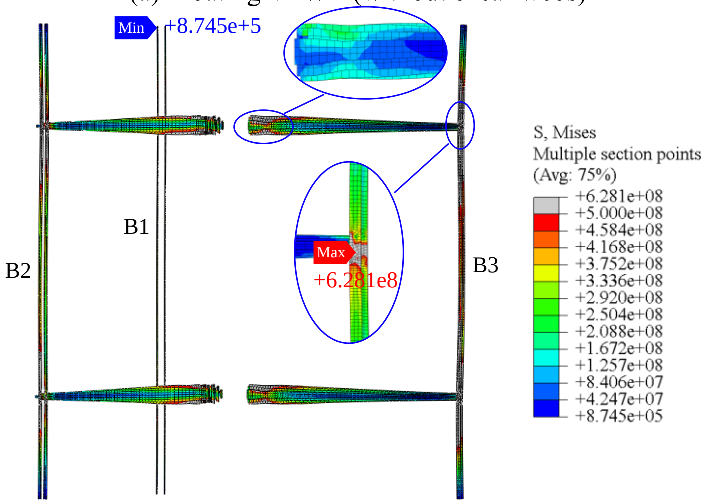

(b) Shear web

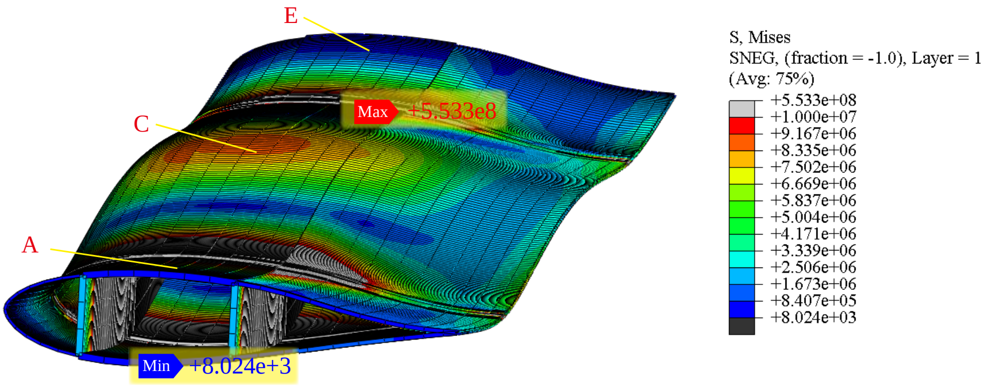

(c) Blade1 (with shear webs)

Fig. 25 Stress distribution and structure deformation of floating VAWT

In Fig. 25c, deformation along the radial direction of the rotor at positions A, C and E of the B1 can be clearly observed. The maximum stress occurs at the connection between the arm's root and the blade, which is about 5.553×10^8 Pa, while the minimum stress is located at the edge of the blade tip, approximately 8.024×10^3 Pa. This indicates that the main deformation region of the blade is located at the middle and ends, caused by both wind force action and the centrifugal forces due to rotation.

5.3.2. Areo-elastic response of blade

Fig. 26 shows the deformation curves for the upper and lower support arms (positions B and D) and various sections of blade 1 (positions A, C, and E). During the start-up to rated speed phase (0-10 s) of the floating VAWT, continuous increases in deformations are noted, with oscillations of 0.53 m for the blade and 0.45 m for the arms. This is due to: (i) the blades being parallel to the rotational axis, which are subjected to rotational centrifugal forces and wind loads causing outward deformations along the rotor's radial direction; (ii) the arms, perpendicular to the axis, experiencing vertical vibrations from their own weight and the gravitational load of the blades.

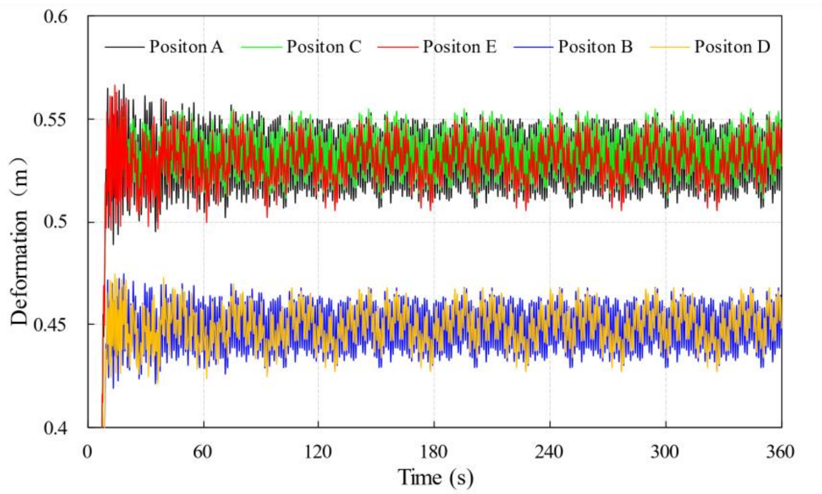

Fig. 26 Variation of deformation for floating VAWT blades and arms

Furthermore, deformation at different blade positions ranges from 0.51 m to 0.56 m, whereas at the arm ends, it oscillates between 0.43 m and 0.47 m. This reveals that blades experience greater deformation than the arms, largely because of the different material properties; the arms are constructed of steel, which is less deformable compared to the blades made from flexible composite materials.

Fig. 27 illustrates the trend of deformation variations at different positions on the blades and struts. It can be observed that during one rotation cycle of the floating VAWT, different positions on the blades (positions A, C, and E) and the ends of the struts (positions B and D) undergo approximately seven reciprocating fluctuations, with consistent phase alignment but varying amplitude differences. Moreover, the deformation fluctuations at positions A, B, and C are more intense compared to positions D and E. This is primarily due to the VAWT tower design featuring a tapered diameter with uniform thickness, where the base of the tower has the largest diameter and the top the thinnest, significantly reducing stiffness at the top and causing more intense vibrations in the upper strut structures. Additionally, the tower's interference with the inflow at the lower parts of the blades is greatest, leading to abrupt fluctuating deformations at position E.

Under wind loads, the deformation vibrations of the blades increase the risk of structural fatigue damage and may even lead to the failure of composite materials. In practical engineering, it is necessary to optimize the connections between different components of the VAWT structure. Employing more advanced blade composite material designs and lay-up schemes is also a potential solution to address the aerodynamic responses of the blades.

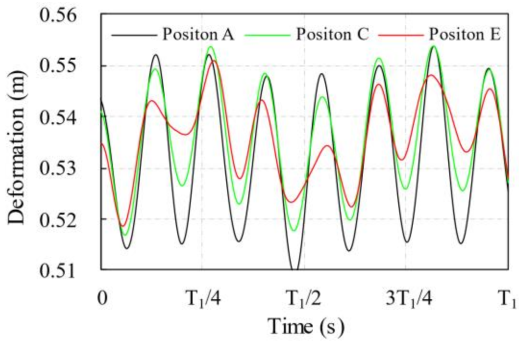

(a) Blade

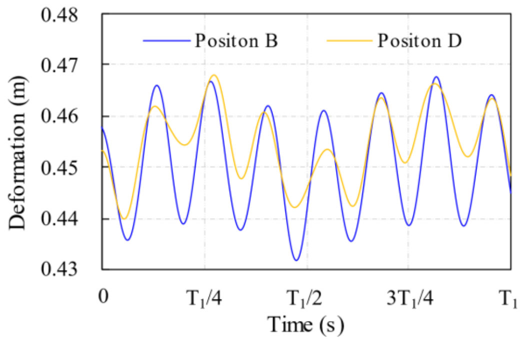

(b) Arms

Fig. 27 Variation of deformation for floating VAWT blades and arms within one rotation period

5.3.3. Contact effect between catenary and seabed

The dynamic response of the platform leads to consistent friction between the catenaries and the seabed, thereby increasing the potential for breakage or damage. It is crucial to analyze the structural behavior of the catenaries to understand and mitigate these risks. Fig. 28 illustrates a schematic diagram of the contact openings between the beam elements Ele1 to Ele3 on the catenaries C1 to C3 and the seabed. The points projected from the midpoints of Ele1 to Ele3 onto the seabed are 800 meters away from the seabed center. As shown in the enlarged view of Fig. 28, the inner side of Ele2 is termed Ele2_in, and the outside is referred to as Ele2_Out.

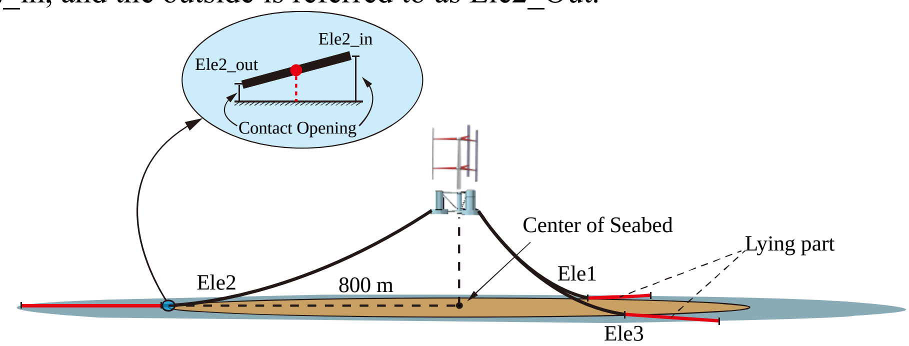

Fig. 28 Schematic diagram of the contact opening between the catenary and the seabed

Fig. 29 shows the contact pressure contours between the catenaries and the seabed. When the floating platform surges toward the negative X-direction (Fig. 29a), catenary C2 becomes slack, thereby increasing the length of the ground-laying section and resulting in a maximum contact pressure with the seabed of approximately 1.206×10^2 Pa. Conversely, when the platform surges toward the positive X-direction (Fig. 29b), catenary C2 is under tension, causing the ground-laying sections of C1 and C3 to extend, with C3 experiencing the highest contact pressure of about 1.156×10^2 Pa. Interestingly, as the platform reciprocates, the peak contact pressures consistently occur between catenaries C2 and C3.

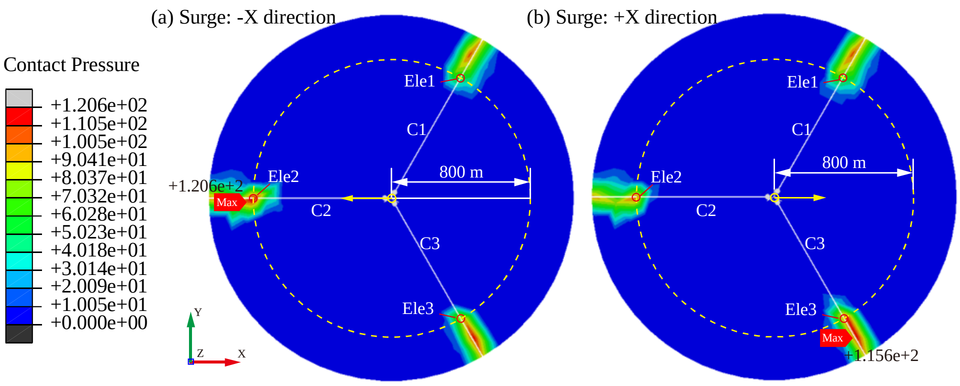

Fig. 29 Contact pressure between catenary and seabed

To better understand the physical reasons which led to these results, a detailed analysis of the contact opening profiles for Ele1-Ele3 was conducted, as depicted in Fig. 30. Remarkable consistency was found between the two data sets for each element, with deviations occurring only at the peaks of the contact opening curves. These deviations, which can be attributed to the contact sequences of the two endpoints for element Ele1 to Ele3, diminish as the mesh density of the catenary increases.

Moreover, the contact opening patterns of Ele1 and Ele3 are completely opposed to that of Ele2. As previously discussed, catenaries C1 and C3 are arranged on opposite sides of catenary C2, resulting in different motion behaviors. More in detail, the fluctuation amplitude of Ele3 exceeds that of Ele1 over the observed time span. This discrepancy stems from the platform's positive roll and sway responses along the Y-axis, consistently maintaining values greater than zero. As a result, the interactions between catenary C3 and the seabed are more pronounced. This phenomenon also accounts for the dynamic shifts in maximum contact pressure observed between catenaries C2 and C3, as depicted in Fig. 29.

It is important to note that the contact opening curve of Ele3 remains above zero, signifying that the region where Ele3 is located never makes contact with the seabed (Fig. 30c). This outcome is triggered by the negative yaw response (clockwise rotation around the Z axis) of the floating VAWT, leading to the torsion of the catenary.

The above results contribute to the understanding of the dynamic behaviors of catenaries in marine settings. Optimizing and reinforcing the structural strength of the region where the catenary interacts with the seabed is crucial for the structural safety of the catenary.

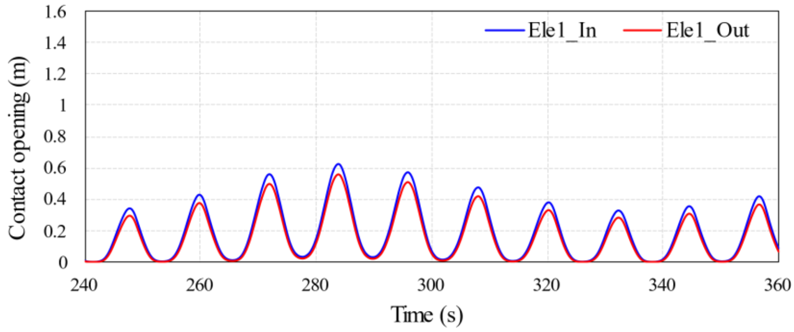

(a) (a) Contact opening for Ele1 of catenary1

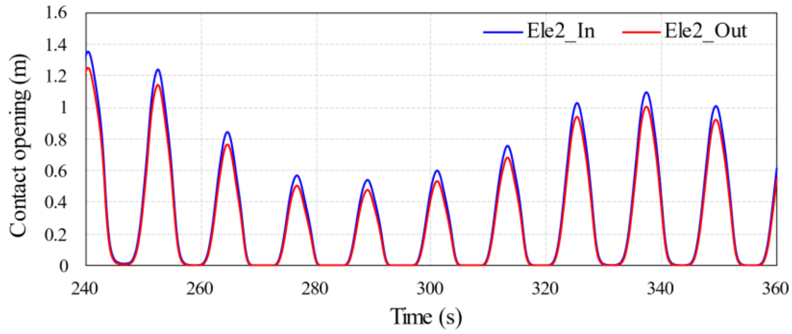

(b) (b) Contact opening for Ele2 of catenary2

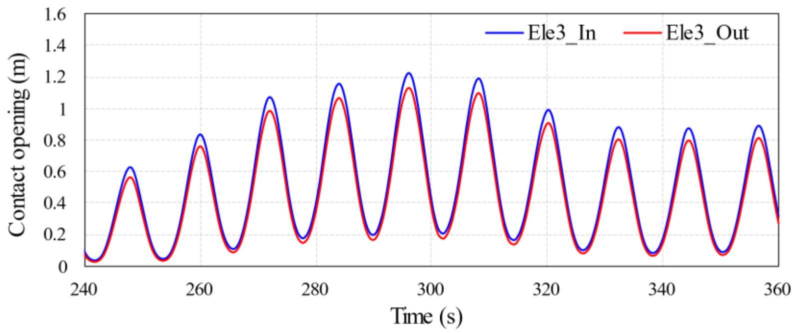

(c) Contact opening for Ele3 of catenary3

Fig. 30 The variation trend of contact opening over time

6. Conclusions

In this paper, a fully coupled aero-elastic-hydro-mooring-material model of a floating VAWT is developed using the CFD-FEM numerical method. Initially, comparative analyses are conducted on the power coefficient and wake characteristics between a floating VAWT and a fixed VAWT with the same rotor configuration. The physical mechanism by which platform motions influence blade torque is obtained. Subsequently, the aeroelastic properties of the floating VAWT blades, the structural stress distribution, and the contact effect between the mooring and the seabed were investigated using the fully coupled model. The main conclusions are summarized as follows:

- The power coefficient of the floating VAWT is approximately 9.3% higher than that of a fixed VAWT at the optimal TSR of 3.28. The power coefficient curve of the floating VAWT exhibits more pronounced fluctuations, displaying many spike-like peaks, largely due to the dynamic response of platform. However, the wake of the floating VAWT dissipates more rapidly and recovers quicker. Within the range of 2≤X/D≤6, the wake velocity of the floating VAWT generally surpasses that of the fixed VAWT. Notably, at X/D=6 and Y/D=0.2, the wake velocity of the floating VAWT increases significantly by about 171% compared to the fixed VAWT. However, at X/D=8, the wake centerline velocity (Y/D=0) of the floating VAWT shows a slight decrease relative to the fixed VAWT. This reduction is primarily due to the reciprocating motion of the floating platform, which boosts the momentum of the low-speed fluid in the distant wake region. Consequently, the fluid velocity at the wake centerline maintains the upstream wake velocity over a relatively longer distance.

- The surge and pitch motions of the platform influence the relative velocity of the blades to the fluid, causing both additive and subtractive interactions with the incoming flow. Specifically, when the platform surges toward the negative X direction and the pitch angle increases, the peak torque of B1 for floating VAWT increases by 27.1% compared to the fixed VAWT. Conversely, when the platform surges toward the positive X direction and the pitch angle decreases, the peak torque of the floating VAWT blades drops by 13.6% relative to the fixed VAWT.
- A stress concentration phenomenon is observed between the built-in shear webs of the support arm and the blade, where stress reaches 6.281×10^8 Pa. This area demands particular attention in engineering applications to prevent structural fatigue and damage. The second highest stress is noted at the bottom of the platform's central pontoon, approximately 3.228×10^8 Pa, attributed to the pontoon bearing the gravity loads of the entire tower and blades. The lowest stress occurs at the blade tips, about 8.024×10^3 Pa. This is primarily because the blade tips are remote from the tower, arms, and other connection points, which are critical regions for transmitting forces and torques between the various components of the VAWT.
- During the acceleration phase to rated speed (0-10 s) of the floating VAWT, the deformation of blade 1 at positions A, C, and E, as well as the two support arms at positions B and D, progressively increased, resulting in reciprocating vibrations of 0.53 m and 0.45 m, respectively. Specifically, the blades deform radially due to wind loads and the centrifugal force of rotation. In contrast, the support arms vibrate in the vertical direction of the VAWT, influenced by their own weight and the gravitational force from the blade. The tower significantly interferes with the inflow to the lower part of the blade, reducing the amplitude of deformation at position E, but with jumping fluctuations.
- The contact opening between the catenaries and the seabed changes dynamically with the platform motion, with the maximum contact pressure alternating between catenaries C2 and C3. Notably, catenary C2 on the windward wave side exhibits a more pronounced contact response with the seabed, reaching a maximum contact pressure of 1.206×10^2 Pa. Additionally, the platform's roll and sway responses induce torsion in the catenaries, resulting in a significant difference in the contact opening curves between C1 and C3.

Future research will investigate the effects of different wave periods, wave heights, and irregular waves on the power coefficient, wake characteristics, blade torque, and structural nonlinearities of floating VAWTs. It should be noted that the OC4 semi-submersible floating platform used in this paper was originally developed for a 5 MW floating HAWT. Due to the unique aerodynamic characteristics and center of mass distribution of floating VAWTs, it is necessary to design and optimize a new type of platform specifically for floating VAWTs, and to validate its effectiveness and economic feasibility.

Acknowledgement

The authors would like to acknowledge the support of National Natural Science Foundation (NSFC) of China (Grant No. 52375193, No. 52106262, No. 52101317and No. 52006148) and is grateful for the financial support (NSFC 51976131). The authors wish to thank the management of High-Performance Computer Cluster-Prospero at LJMU, which provided abundant computational resources for this research.

References

[1] Hand B, Cashman A. A review on the historical development of the lift-type vertical axis wind turbine: From onshore to offshore floating application. Sustainable Energy Technologies and Assessments, 2020, 38: 100646.

[2] Ahsan F, Griffith D T, Gao J. Modal dynamics and flutter analysis of floating offshore vertical axis wind turbines. Renewable Energy, 2021, 185: 1284-1300.

[3] Subbulakshmi A, Verma M, Keerthana M, et al. Recent advances in experimental and numerical methods for dynamic analysis of floating offshore wind turbines — An integrated review, Renewable and Sustainable Energy Reviews, 2022, 164: 112525.

[4] Borg M, Shires A, Collu M. Offshore floating vertical axis wind turbines, dynamics modelling state of the art. part I: Aerodynamics. Renewable and Sustainable Energy Reviews, 2014, 39: 1214-1225.

[5] Tjiu W, Marnoto T, Mat S, et al. Darrieus vertical axis wind turbine for power generation I: Assessment of Darrieus VAWT configurations. Renewable Energy, 2015, 75: 50-67.

[6] Ottermo F, Bernhoff H. An upper size of vertical axis wind turbines. Wind Energy, 2015, 17(10): 1623-1629.

[7] Griffith D T, Barone M, Paquette J, et al. Design studies for deep-water floating offshore vertical axis wind turbines. Sandia National Laboratories Technical Report, SAND2018-7002, 2018.

[8] Griffith D T, Paquette J, Barone M, et al, A study of rotor and platform design trade-offs for large-scale floating vertical axis wind turbines. Journal of Physics Conference Series, 2016, 753: 102003.

[9] Sutherland H J, Berg D E, Ashwill T D. A Retrospective of VAWT Technology. Sandia National Laboratories Technical Report, SAND2012-0304, 2012.

[10] Ennis B L, Griffith D T. System levelized cost of energy analysis for floating offshore vertical-axis wind turbines. Sandia National Laboratories Technical Report, SAND2018-9131, 2018.

[11] Vita L, Paulsen U S, Perdersen T F, et al. Rasmussen F. A novel floating offshore wind turbine concept. The European wind energy conference, Marseille, France: EWEC, 2009.

[12] Vita L. Offshore vertical axis wind turbine with floating and rotating foundation. Technical University of Denmark, 2011.

[13] Berthelsen P A, Fylling I, Vita L, et al. Conceptual design of a floating support structure and mooring system for a vertical axis wind turbine. Proceedings of the ASME International Conference on Ocean, Offshore and Arctic Engineering, 2012.

[14] Cahay M, Luquiau E, Smadja C, et al. Use of a vertical wind turbine in an offshore floating wind farm. Offshore Technology Conference, 2011.

[15] Pitance D, Horb S, Bordier J K, et al. Experimental validation of pharwen code using data from vertical axis wind turbines. WindEurope, 2016.

[16] SKWID. Floating Wind & Current Hybrid Power Generation–Savonius Keel & Wind Turbine Darrieus; 2013.

[17] Tran T T, Kim D H. Fully coupled aero-hydrodynamic analysis of a semi-submersible FOWT using a dynamic fluid body interaction approach. Renewable Energy, 2016, 92: 244-261.

[18] Liu Y, Xiao Q, Incecik A, et al. Establishing a fully coupled CFD analysis tool for floating offshore wind turbines. Renewable Energy, 2017, 112:280-301.

[19] Yang Yang, Musa Bashir, Constantine Michailides, et al. Development and application of an aero-hydro-servo-elastic coupling framework for analysis of floating offshore wind turbines. Renewable Energy, 2020,161 (23):606-625.

[20] Yang Yang, Musa Bashir, Constantine Michailides, et al. Coupled analysis of a 10 MW multi-body floating offshore wind turbine subjected to tendon failures. Renewable Energy, 2021, 176(21), 89-105.

[21] Yang Yang, Musa Bashir, Jin Wang, et al. Performance evaluation of an integrated floating energy

system based on coupled analysis. Energy Conversion and Management, 2020, 223(21):113308.
[22] Robert H, Qin, N, Jonathan E, et al. Wind tunnel and numerical study of a small vertical axis wind turbine. Renewable Energy, 2010, 35: 412-422.
[23] Marco R C, Alessandro E, Ernesto B. The Darrieus wind turbine: Proposal for a new performance prediction model based on CFD. Energy, 2011, 36: 4919-4934.
[24] LI Q A, Maeda T, Kamada Y, et al. Wind tunnel and numerical study of a straight-bladed vertical axis wind turbine in three-dimensional analysis (Part I: For predicting aerodynamic loads and performance. Energy, 2016: 106: 443–52.
[25] Liu Q S, Miao W P, Bashir M, et al. Aerodynamic and aeroacoustic performance assessment of a vertical axis wind turbine by synergistic effect of blowing and suction. Energy Conversion and Management. Energy Conversion and Management, 2022, 217: 116289.
[26] Wang Z Y, Wang Y C, Zhuang M. Improvement of the aerodynamic performance of vertical axis wind turbines with leading-edge serrations and helical blades using CFD and Taguchi method. Energy Conversion and Management, 2018, 177: 107-121.
[27] Zuo W, Wang X, Kang S. Numerical simulations on the wake effect of H-type vertical axis wind turbines. Energy, 2016, 104: 295-307.
[28] Dong Z K, Chen Y R, Zhou D, et al. The mean wake model and its novel characteristic parameter of Hrotor VAWTs based on random forest method. Energy, 2022, 239: 122456.
[29] Abdolrahim R, Hamid M, Bert B. CFD analysis of dynamic stall on vertical axis wind turbines using Scale-Adaptive Simulation (SAS): Comparison against URANS and hybrid RANS/LES. Energy Conversion and Management, 2019, 196: 1282-1298.
[30] Balduzzi F, Bianchini A, Ferrara G, et al. Dimensionless numbers for the assessment of mesh and timestep requirements in CFD simulations of Darrieus wind turbines. Energy, 2016, 97: 246-261.
[31] Balduzzi F, Bianchini A, Maleci R, et al. Critical issues in the CFD simulation of Darrieus wind turbines. Renewable Energy, 2016, 85: 419-435.
[32] Abdolrahim R, Ivo K, Bert B, et al. CFD simulation of a vertical axis wind turbine operating at a moderate tip speed ratio: Guidelines for minimum domain size and azimuthal increment. Renewable Energy, 2017, 107: 373-385.
[33] Balduzzi F, Drofelnik J, Bianchini A, et al. Darrieus wind turbine blade unsteady aerodynamics: a three-dimensional Navier-Stokes CFD assessment. Energy, 2017, 128: 550-563.
[34] Bianchini A, Balduzzi F, Ferrara G, et al. A computational procedure to define the incidence angle on airfoils rotating around an axis orthogonal to flow direction. Energy Conversion and Management, 2016, 126: 790-798.
[35] Bianchini A, Balduzzi F, Ferrara G, et al. Virtual incidence effect on rotating airfoils in Darrieus wind turbines. Energy Conversion and Management, 2016, 111: 329-338.
[36] Lei H, Zhou D, Bao Y, et al. Numerical simulations of the unsteady aerodynamics of a floating vertical axis wind turbine in surge motion, Energy, 127 (2017): 1-17.
[37] Su J, Chen Y, Han Z, et al. Aerodynamic performance assessment of 4-type vertical axis wind turbine under pitch motion, Energy, 225 (2021): 120202.
[38] Kuang L, Lu Q, Huang X, et al. Characterization of wake interference between two tandem offshore floating vertical-axis wind turbines: Effect of platform pitch motion, Energy Conversion and Management, 265 (2022): 115769.
[39] Owens B C, Hurtado J E, Aeroelastic Modeling of Large Offshore Vertical-axis Wind Turbines: Development of the Offshore Wind Energy Simulation Toolkit. In: Proceedings of the 54th AIAA/ASME/ASCE/AHS/ASC structures, structural dynamics, and materials conference, Boston, USA
[40] Collu M, Borg M, Shires A, et al. FloVAWT: Progress on the Development of a Coupled Model of Dynamics for Floating Offshore Vertical Axis Wind Turbines, Proceedings of the ASME 2014, San Francisco
[41] Antonutti R. Numerical Study of Floating Wind Turbines: Hydro- and Aero-mechanics, PhD

Thesis, 2015, The University of Edinburgh
[42] Wang K, Moan T, Hansen M O L. Stochastic dynamic response analysis of a floating vertical-axis wind turbine with a semi-submersible floater, Wind Energy. 2016, 19: 1853–1870.
[43] Cheng Z, Wang K, Ong M C. Assessment of performance enhancement of a semi-submersible vertical axis wind turbine with an optimized Darrieus rotor, Engineering Structures, 2018, 167: 227–240.
[44] Luo W, Liu W, Yang M, et al. Load Characteristics and Extreme Response of Straight-Bladed Floating VAWT Using a Fully Coupled Model, Journal of Marine Science and Engineering, 2023, 11(1): 185.
[45] Ayati A, Steiros K, Miller M, et al. A double-multiple streamtube model for vertical axis wind turbines of arbitrary rotor loading, Wind Energy Science, 2019, 4: 653-662.
[46] Xu K, Shao Y, Gao Z, et al. A study on fully nonlinear wave load effects on floating wind turbine. Journal of Fluids and Structures. 2019, 88: 216-240.
[47] Borg M, Collu M, Kolios A. Offshore floating vertical axis wind turbines, dynamics modelling state of the art. Part II: Mooring line and structural dynamics. Renewable and Sustainable Energy Reviews, 2014, 39: 1226-1234.
[48] Borg M, Collu M, Kolios A. Offshore floating vertical axis wind turbines, dynamics modelling state of the art. Part II: Mooring line and structural dynamics. Renewable and Sustainable Energy Reviews, 2014, 39: 1226-1234.
[49] Fenton, John D. A Fifth-Order Stokes Theory for Steady Waves, Journal of Waterway, Port, Coastal, and Ocean Engineering, 1985, 111 (2): 216-234.
[50] Choi J, Sung B Y. Numerical simulations using momentum source wavemaker applied to RANS equation model, Coastal Engineering. 2009, 56 (10): 1043-1060.
[51] Soeb M, Islam A B M, Jumaat M Z, et al. Response of nonlinear offshore spar platform under wave and current. Ocean Engineering, 2017, 144: 296-304.
[52] Hand B, Cashman A. Conceptual design of a large-scale floating offshore vertical axis wind turbine, 9th International Conference on Applied Energy, 2017, ICAE2017, 21-24, Cardiff.
[53] Robertson A, Jonkman J, Masciola M, et al. Definition of the Semisubmersible Floating System for Phase II of OC4, Technical Report TP-5000-60601, 2014, NREL, Colorado.
[54] Hand B, Kelly G, Cashman A. Structural analysis of an offshore vertical axis wind turbine composite blade experiencing an extreme wind load, Marine Structures, 2020, 75: 102858.
[55] Taylor R and Valent P, 1984. Design Guide for Drag Embedment Anchors, Naval Civil Engineering Laboratory (USA), TN No N-1688.
[56] Miao W, Li C, Wang Y, et al. Study of adaptive blades in extreme environment using fluid–structure interaction method. Journal of Fluids and Structures, 2019, 91: 102734.
[57] Battisti L, Persico G, Dossena V, et al. Experimental benchmark data for H-shaped and troposkien VAWT Architectures, Renewable Energy, 2018, 125: 425-444.
[58] Cheng P, Huang Y, Wan D, et al. A numerical model for fully coupled aero-hydrodynamic analysis of floating offshore wind turbine. Ocean Engineering, 2019, 173: 183-196.
[59] IEC 61400-1 Wind turbine generator systems - Part 1: Safety Requirements. Tech report, International Electrotechnical Commission.